ANALYZING SUPERCELL INTENSITY CHANGES IN A HETEROGENEOUS ENVIRONMENT IN THE VORTEX2 SUPERCELL PAIR IN SOUTHEASTERN COLORADO ON 11 JUNE 2009

by

Cody James Ledbetter

A thesis submitted to the faculty of
The University of North Carolina at Charlotte
in partial fulfillment of the requirements
for the degree of Master of Science in
Earth Science

Charlotte

2018

Approved by:

_____

Dr. Casey Davenport

_____

Dr. Matthew Eastin

_____

Mr. Terry Shirley

ABSTRACT

CODY JAMES LEDBETTER: Analyzing supercell intensity changes in a heterogeneous environment in the VORTEX2 supercell pair in southeastern Colorado on 11 June 2009 (Under the direction of DR. CASEY DAVENPORT)

Predicting supercell thunderstorm evolution in strongly-forced environments is relatively well-understood. However, this is not always the type of environment that spawns supercells. In fact, some supercell environments can be quite complex in nature. A variety of environmental complexities are possible, including interactions with frontal boundaries, merging with other storms, the presence of high shear-low CAPE (HSLC) environments, and the nocturnal transition; each of these scenarios can produce temporal and spatial variations in key quantities of instability, shear, and helicity. The goal of this study is to do an in-depth mesoscale analysis of a pair of supercells examined during the VORTEX2 project in southeastern Colorado on the evening of 11 June 2009, with the goal of determining what environmental factors lead to intensity changes within the supercell pair. This will be done by combining environmental data, primarily upper air sounding launches performed by both VORTEX2 researchers and the National Weather Service (NWS) office in Dodge City, KS, as well as radar data in the form of both NEXRAD level II radar data from NWS Pueblo, CO and mobile radar data from Doppler-on-wheels (DOW) and Shared Mobile Atmospheric Research and Teaching Radar (SMART) radars. Mobile radar data will be used to perform a dual-Doppler analysis in order to calculate 3-dimensional wind and vorticity fields for the cells. These datasets will be compared with one another, as well as previous research, in order to try to determine if any, or all, aspects of this storm's environment, attribute to any of the intensity fluctuations in either supercell. Overall, the fluctuations during and after the

merger begins between to occur between the two supercells were more intense compared to those before the merger occurred. This could be linked to the merger itself, or to the favorable amounts of shear in the inflow environment throughout the analysis period. Additionally, there seemed to be a direct relationship between increasing mesocyclone strength at the mid-levels and LSR occurrences. This would make some sense, given that the rotation is somewhat indicative of increased updraft strength. Lastly, as consistent with previous research, the period just following the beginning of the merger seemed to be an inflection point that marked a significant increase in mesocyclone strength at all levels. During the merger period, there are several instances of low-level rotation as well, which also would tend to indicate some strengthening, since rotation was able to extend down towards the surface. Dual-Doppler data seemed to only affirm these trends, as most trends in updraft and vertical vorticity strength and size seemed to be consistent with that of mesocyclone intensity and depth.

ACKNOWLEDGEMENTS

I would like to first thank my advisor Dr. Casey Davenport for bringing me into her research group as a master's student. I greatly appreciate everything you have done to help guide me into finishing this project. You were a great advisor and always made sure I was getting things done, but never go impatient when I didn't get things done exactly on time. None of this would have been possible without your help, so thank you. Also, I would like to thank my thesis committee members, Terry Shirley and Dr. Matthew Eastin, who provided many helpful help and suggestions for my project along the way. A special thanks also goes out to Matthew Gropp, Warren Pettee and Alexander Schaefer, who were a huge help in helping me learn how to use coding for some aspects of my project, and for that I am eternally grateful. I would also like to thank my parents Anna Hopkins, Neal and Misty Ledbetter for their support and motivation throughout this process. Finally, I would like to thank all of my close friends, who can not all be named, for their support and motivation throughout this process.

TABLE OF CONTENTS

LIST OF TABLES

LIST OF FIGURES

CHAPTER 1. INTRODUCTION

The genesis and maintenance of supercell thunderstorms is relatively well-understood, particularly in strongly-forced environments. However, many supercells do not form in such clear-cut environments, making forecasting much more difficult. A variety of environmental complexities are possible, including interactions with frontal boundaries, merging with other storms, the presence of high shear-low CAPE (HSLC) environments, and the nocturnal transition; each of these scenarios can produce temporal and spatial variations in key quantities of instability, shear, and helicity. Many studies have sought to understand how supercell thunderstorms are influenced by these scenarios, but what happens if a supercell is within an environment containing several of these complexities? Which of these complexities, if any, will have the most impact on strengthening and weakening phases in a supercell? The primary goal of this research is to evaluate the response of observed supercells subject to multiple external factors influencing the local storm environment; this will be achieved by utilizing a suite of observational data to quantify changes in storm intensity and severity. The present study will focus on a pair of supercell thunderstorms that were observed during the Verification of the Origin of Rotation in Tornadoes Experiment 2 (VORTEX2; Wurman et al. 2012) field campaign near La Junta, Colorado on 11 June 2009. This set of supercells was chosen due to the wide range of factors influencing the inflow environment of this pair of supercells.

The parent supercell (Cell A) in this supercell pair was initiated off of a stationary front in the lee of the Rocky Mountains around 2030 UTC on 11 June 2009 (Fig. 1). As the evening progressed, this supercell quickly moved away from the stationary front. Along this same stationary front, and perhaps with the help of the outflow boundary of Cell A, another supercell (Cell B) formed due south of Cell A at around 2251 UTC (shown in Fig. 2 later in its lifetime at around 2310 UTC in order to better exemplify its structure). The intensity of both cells prompted several severe thunderstorms and tornado warnings, verified by numerous local storm reports (Fig. 3). Eventually, the two cells merged into one complex (Cell C) by 0128 UTC (Fig. 4). As this occurred, the nocturnal transition began, resulting in the inflow environment becoming increasingly stable yet more highly sheared. This case thus epitomizes a situation with numerous environmental complexities, each of which may produce varying effects on supercell intensity and behavior.

This event was the focus of an intensive observing period during the VORTEX2 field campaign, resulting in a large amount of observational data for analysis. The present study will primarily focus on data gathered from weather balloons launched in the inflow environment, as well as mobile and fixed Doppler radars; this will allow for an assessment of the changes in the inflow and mesoscale environments and their subsequent influence on story intensity and evolution.

CHAPTER 2. LITERATURE REVIEW

To provide context for analysis of the 11 June 2009 event, a discussion of various external factors that influence supercell intensity and evolution will be described, with a focus on storm mergers, the nocturnal transition, and HSLC environments. However, before discussing how supercells are modified by different external factors in their environment, it is crucial to have a basic understanding of how supercells work on their own, and in what type of environment that they generally form.

Development and maintenance of discrete supercells is pretty well-understood, as well as how they generally propagate. The two big environmental factors to take into account are instability and shear. These are the two primary building blocks for supercell thunderstorms, along with moisture, which is needed for any thunderstorm to form and be maintained. Generally, CAPE values of 2000 J/kg or greater are sufficient for supercell development and maintenance. A lifting mechanism is also needed, whether it be to reach the convective temperature, a cold front pass through, etc. Then, the level of free convection (LFC) must also be low enough for the lifting mechanism to lift a parcel into the buoyant air. Also, CIN should also be fairly low for the formation and maintenance of supercells.

Wind shear is the next key component to supercell development and maintenance. Several past and recent studies have shown that vertical wind shear is directly related to supercell development, intensity, and maintenance (e.g., Lemon and Doswell 1979; Rotunno and Klemp 1985; Weisman and Rotunno 2000; Bunkers et al. 2006a; Coffer and

Parker 2015). From Bunkers et al. 2006a, it was found that most long-lived supercells were in environments with 20 m/s to 40 m/s of 0-8 km shear, with the strongest existing in environments with the highest shear values. Vertical wind shear creates a rolling tube of horizontal shear, which can then become tilted into the vertical by updrafts in a thunderstorm (Fig. 5), which marks the beginning of mid-level rotation in supercells.

Once this occurs, the next question becomes "which cell, if not both, is favored during the splitting process?" The answer to this question has everything to do with directional shear and can be split up into three categories: mirrored supercell, right mover, and left mover. If a straight hodograph is observed, mirrored supercells will be favored, but if a clockwise-turning (counter-clockwise-turning) hodograph is observed, right-moving (left-moving) supercells will be favored (Fig. 6). The reason for these tendencies can be explained by the vertical perturbation pressure gradient force (VPPGF; Fig. 7). In the case of the straight hodograph (Fig. 7a), the shear vector causes high perturbation pressure to build on the upwind side of the updraft, while low perturbation pressure builds on the downwind side of the updraft. So upward motion is favored ahead of both mid-level mesocyclones in the supercell, meaning that both storms can maintain themselves. However, in the clockwise hodograph case (Fig. 7) the horizontal PGF turns with height, leading to an upward VPPGF to the right of the shear vector, and an area of downward VPPGF to the left of the shear vector. This allows for the right mesocyclone to dominate and the left storm to dissipate.

2.1 Supercells Undergoing Merging Events

While storm interactions with other cells are common, previous research shows a wide range of impacts on storm morphology. For example, Wurman et al. (2007)

performed a case study of merging cells on tornadogenesis, where two different mergers occurred (Fig. 8). Utilizing dual-Doppler analysis to examine the 3D wind field, it was revealed that short-lived tornadoes immediately resulted from each merger; however, the storm quickly weakened after that point. This weakening after the merger, in both cases, was linked to precipitation and cool air invading the updraft region, not allowing for the storms to maintain themselves. In the same vein, Rogers and Weiss (2007) examined radar data from ten prolific tornado producing days between 1999 and 2006, focusing on characteristics of cell mergers that produced tornadoes. It was determined that the optimal merging point for producing tornadoes is west and north of the primary updraft, while non-tornadic mergers occurred much closer to the parent updraft (Fig. 9). It was hypothesized that a merger farther from the updraft reduced the effects of precipitation loading, which acts to reduce buoyancy and retard stretching of vertical vorticity.

French and Parker (2012) examined merger events of a different scale, focusing on supercells merging with well-organized squall lines. As in previous studies, merger events were associated with an increasing severe threat; notably, the strength of forcing was a factor. Weakly forced environments, characterized by a weak 500 hPa trough and a weak or non-existent surface cyclone, favored damaging winds during and just after the merger occurred, and weaker tornadoes after the merger occurred, while strong forcing environments, characterized by a high-amplitude 500 hPa trough and a mature surface cyclone, favored stronger tornadoes and damaging winds prior to the merger. However, unlike previous studies, French and Parker (2012) found that tornadogenesis was less linked to the merger itself; rather, the background environmental conditions were important. These observational studies on supercell mergers illustrate that a merger is a

key inflection point in a supercells' life cycle. Often right around the time of the merger, an increase in severe weather can occur, followed by potential weakening. However, a key question is whether this intensification/weakening pattern is moderated in any way by shifts in the inflow environment; for example, would an increase in low-level shear during the period of merging counteract subsequent weakening? The study herein will help to answer this question.

To complement these observational studies on merging supercells, modeling-based studies have also been conducted to examine the influence of initial spacing of storms on the merging process, as well as the orientation of the wind shear vector. In Bluestein and Weisman (2000), idealized model simulations illustrated that supercell intensity, longevity, and motion were sensitive to the orientation of the vertical shear profile with respect to the orientation of the line along which convection was initiated. It was determined that an angle of 45 degrees or 135 degrees was the ideal angle of shear relative to the line of forcing for longer-lived lines of discrete supercells (Fig. 10a). This resulted less merging cells, which allowed for less contamination of downdrafts of individual cells. In contrast, when the shear was normal or parallel to the line of forcing, things differed, with isolated supercells forming on the ends of a more multicellular squall line (Fig. 10b). This would lead to more interference of individual updrafts due to merging cells interfering with the development of one another. Storms wouldn't necessarily weaken, but would just not maintain their individual structure, but would evolve into a multicell line.

Hastings and Richardson (2016) looked past the short-term effects of mergers on supercell morphology and performed a series of idealized simulations to investigate the

long-term morphological changes of supercells merging with a nascent cell. These simulations involved introducing several warm bubbles into an environment favorable for right-moving supercells. Similar to Rogers and Weiss (2007), the way a merger affects supercell intensity and evolution is heavily dependent on where the interaction takes place relative to the supercell updraft. Hastings and Richardson (2016) found that where the merger occurs, and how the two cells evolve afterwards, is dependent on how far the updraft maxima are spaced apart, referred to as the minimum spacing. Broadly, in cases with no cold pool surges, three solutions could be found. First off, the original cell could just dissipate (Fig. 11a). If minimum spacing between the two updrafts was 20 km, meaning that cells were spaced apart by at least this much, this resulted in the updrafts not joining, allowing for the potential to reform into one supercell (Fig. 11b). If the minimum spacing is less than 10 km the result is an updraft collision, with the storm then continuing as a classic or high precipitation supercell (Fig. 11c). Now, in the case that the updrafts are spaced apart by 10-20 km, things can go a couple of different ways, due in large part to the cold pool surges that come with this interaction because of precipitation from one cell interacting with the updraft of the other. If the new cell that is merging with the parent cell is fairly strong, then a rear inflow jet may begin to form within the storm (Fig. 12a). However, if this new cell is weak, then the original cell will likely continue as a high precipitation (HP) supercell (Fig. 12b). Finally, the broad conclusion was made that rear flank mergers result in stronger mesocyclones (by 300-400%), meaning that cells that merge in the rear flank tended to gain strength. The key result to come from this paper was that none of the mergers situations in this paper resulted in the dissipation of

both storms. In fact, most of them resulted in a storm of comparable or greater strength than the control storm.

As has been shown, several studies have investigated the effects of supercells merging with other types of convection (e.g. multicellular lines and nascent cells). However, far less research has been done on how supercells react when merging with one another. This is a gap that the present study can begin to fill, and hopefully prompt more studies on this topic.

2.2 Supercell Evolution During the Nocturnal Transition

The nocturnal transition involves changes to the thermodynamic and kinematic structure of the atmosphere, occurring near sunset within the atmospheric boundary layer (Fig. 13; Stull 1988). During the nocturnal transition, the temperature within the boundary layer decreases at a rate dependent on many environmental conditions, such as cloud cover, relative humidity, and precipitation. This results in an increase in low-level stability; an increase in vertical wind shear can also occur if the low-level jet develops. Supercell thunderstorms owe their existence to significant vertical wind shear, so these storms may continue to be maintained during the nocturnal transition despite an increase in stability.

Nowotarski et al. (2011) utilized idealized numerical simulations to test the sensitivity of development of low-level rotation in supercell thunderstorms initiated above a horizontally-homogeneous stable boundary layer. By varying the depth and lapse rate of the stable boundary layer, it was found that low-level baroclinic vorticity and stretching of vertical vorticity were reduced in each case, thus weakening near surface rotation; the degree of weakening was modulated by the strength and depth of the stable

layer (Fig. 14). Notably, however, surface parcels were able to be ingested into the main updraft in each simulation, supporting the notion of a dynamically stable mesocyclone via the vertical perturbation pressure gradient force.

Davenport and Parker (2015a) examined the characteristics of an isolated supercell during VORTEX2 that moved into an increasingly stable low-level environment. The storm was initiated by a preexisting frontal boundary, but over time traveled deeper into the stable air, eventually dissipating (Fig. 15). Accordingly, low-level convective inhibition (CIN) increased; deep-layer shear was also observed to weaken. Interestingly, the elevated environment became more favorable over time, with weakening CIN and increasing low-level shear and SRH (Table 1). To assess why the supercell was not sustained as an elevated storm, a follow-up idealized modeling study was conducted that incorporated the observed changes to the inflow environment (Davenport and Parker 2015b). It was shown that changes in both the thermodynamic and kinematic profiles contributed to dissipation by encouraging a shifting updraft parcel source region (Fig. 16). Unsurprisingly, however, thermodynamic variations have a stronger influence than kinematic variations.

Coffer and Parker (2015), using the same idealized modeling technique as Davenport and Parker (2015b), simulated other cases from VORTEX2 where the low-level shear significantly increased, associated with the development of the low-level jet during the nocturnal transition. Importantly, the strong increases in low-level shear over time led to increases in vertical vorticity (Fig. 17a) and intensifying the low-level updraft (Fig. 17b), likely explaining the climatological maximum in tornado frequency around the early-evening transition.

Gropp and Davenport (2018) provided a more comprehensive assessment of supercells during the nocturnal transition; the study categorized originally isolated supercells based on their evolution during the nocturnal transition, taking one of four possible paths: 1) dissipate, 2) merge with other forms of convection, 3) grow upscale to a larger form of convection, or 4) maintain strength through becoming elevated, or remaining surface-based. In all categories, the near-inflow CIN and SRH increased, and CAPE decreased, as expected. However, the maintained and merger cases saw the highest magnitudes of kinematic parameters, but only the maintained cases showed an increase in effective SRH throughout the nocturnal transition. These results suggest a balance between increasing stability and updraft rotation (represented by SRH) is necessary to maintain the VPPGF; stronger updraft rotation will allow dynamic lifting of parcels despite low level stability in maintained cases, agreeing with results found in Nowotarski et al. (2011). Upon completing the statistical analyses of several convective parameters, it was found that the largest differentiation between the development had to do with the effective storm relative helicity (effective SRH), as well as the most unstable convective inhibition (MUCIN).

2.3 High-Shear Low CAPE Environments

Thunderstorm environments with large vertical wind shear but small instability are fairly common across the U.S., and can be present during the nocturnal transition (e.g., Markowski and Straka 2000). McCaul and Weisman (2001) showed that all the basic storm intensity parameters, such as updraft intensity, peak midlevel and surface vorticity, and surface cold outflow, exhibit sensitivity to variations in the shapes of both the buoyancy and wind profiles. In a low-CAPE, or a low-shear environment, if the

buoyancy and shear was concentrated into the lower levels of the troposphere, then that could compensate for that lack of buoyancy and/or shear.

Guyer and Dean (2010) conducted the first climatological study of tornadoes occurring in weakly buoyant (MLCAPE < 500 J/kg) environments. Compared to tornadoes in higher-CAPE environments, tornadoes occurring in weak CAPE environments were more common during the cool season across the U.S. and tended to occur in the overnight hours. Expanding upon the climatology of Guyer and Dean (2010), Sherburn and Parker (2014) examined all types of severe weather occurring within HSLC environments; it was found that significant tornadoes and winds are favored in the southeast during the cool season and becomes more of a hail/wind threat in the Plains in the late spring/early summer. Even this study concludes that low-level features, primarily wind shear, seem to be the real key to supercell intensity in these HSLC environments. This study provided 2 new parameters, called the severe hazards in environments with reduced buoyancy parameter using 0-3 km shear (SHERBS3) and using effective shear (SHERBE), which were found to be more effective to use when forecasting severe weather in HSLC environments than the majority of parameters that we can currently use (Fig. 18). The SHERB parameters combine the 0-3 km lapse rate, the 700-500 hPa lapse rate, and either the effective (SHERBE), or the 0-3 km shear (SHERBS3) in order to create a composite parameter to predict whether or not a storm that forms in HSLC environments will produce significant severe reports. Note that this parameter is not a tool for forecasting convection, but rather how severe that convection might become.

2.4 Putting it all Together

The individual effects of various environmental factors on supercell development and evolution have been well-studied. In environments with merging supercells, it is quite clear that the time leading up to, and just following, the merge point is a key time for increased severe potential, followed typically by a weakening phase. Additionally, the position of the merger is key in determining subsequent changes to intensity and likelihood of producing tornadoes. However, many of these previous studies have primarily focused on supercells interacting with multicellular lines or nascent cells. So, a gap exists in relation to how supercells react to merging with one another, which is a gap that the present study looks to begin to fill. The nocturnal transition is well-understood to modulate supercell intensity, behavior, and morphology; on the one hand, less CAPE and more CIN can weaken convection, while increases in shear can allow for supercell intensification and even tornadogenesis. This increase in shear is key, as HSLC environments present their own forecasting challenges. The present study presents a unique opportunity to study all these features interacting with a pair of supercells over a period of a couple hours, taking advantage of a breadth of observational data from the VORTEX2 campaign.

CHAPTER 3. DATA AND METHODS

3.1 Environmental Data

During the VORTEX2 field campaign, the near-inflow environment of target supercells was observed via radiosondes throughout the storm's lifetime. For the 11 June 2009 case, a total of thirteen soundings were collected from the near and far inflow regions, as well as the forward and rear flank downdraft regions. This study will primarily focus on the four soundings that collected information on the inflow environment of both supercells, largely favoring the southern storm (Cell B) (Fig. 19). These launches occurred over the course of a few hours, capturing environmental shifts during the nocturnal transition, allowing for connections to be made between the changing environment and subsequent storm behavior. These soundings and their associated hodographs are pictured in Figs. 20 and 21 respectively, with vertical profiles of CAPE and CIN shown in Fig. 22. To supplement these inflow soundings, a sounding was also collected from the National Weather Service (NWS) office in Dodge City, KS (Fig. 23). This sounding can give a good sample of what type of environment the storm was moving into, but where there has been no influence from the storm itself. Secondarily, the soundings located within the rear flank downdraft (RFD) region (Fig. 24) will be used to help better understand the environment behind the outflow boundary of Cell A/A'. The RFD soundings specifically will give insight as to how the gust front from Cell A/A' interacts with and affects the evolution of Cell B/B', which will be

described later in the results. The RFD soundings and associated hodographs can be seen in Figs. 25 and 26 respectively, with vertical CAPE and CIN profiles pictured in Fig. 27.

Note that some soundings did not reach the tropopause; to provide an adequate comparison of integrated parameters (e.g., convective available potential energy), incomplete soundings utilized upper-level information from the next-closest sounding in both time and space. For example, the 2329 UTC sounding was completed by the 0014 UTC sounding (e.g., compare Fig. 20a and b). It is assumed here that the upper-levels contain weaker spatial and temporal gradients, resulting in only a small amount of error in the integrated calculations. Even with this assumption, these soundings are the best possible representation of the atmosphere with the available observational data. As for the RFD soundings, since all soundings reached the height of the equilibrium level (EL), this same procedure was not performed.

Visualization of the soundings, along with numerous convective parameters (e.g. convective available potential energy [CAPE], convective inhibition [CIN], storm relative helicity [SRH], lifted index [LI], supercell composite parameter [SCP], significant tornado parameter [STP], etc.) was achieved through SHARPpy (Blumberg et al. 2017). These parameters are designed to quantify the thermodynamic and kinematic info environment and its evolution over time. Additionally, vertical distributions of CAPE and CIN were also created for each sounding to identify the potential for the storms becoming elevated during the nocturnal transition (e.g., Davenport and Parker 2015a; Gropp and Davenport 2018). These vertical distributions were achieved by calculating the CAPE and CIN of a parcel at every single level in the sounding to create a vertical profile.

3.2 Radar data

Overall, the present study seeks to understand how complexities within the environment of a supercell thunderstorm affect storm intensity and evolution. To quantify changes to the supercells as a result of the complex environment on 11 June 2009, this study will utilize mobile and WSR-88D radar data. These data were collected by the following mobile radars during the VORTEX2 field campaign: Doppler-on-Wheels 6 and 7 (DOW-6, DOW-7; Wurman et al. 1997, Wurman 2001), Shared Mobile Atmospheric Research and Teaching Radar 1 (SMART-R1 & SMART-R2; Biggerstaff et al. 2005), as well as the WSR-88D in Pueblo, Colorado (KPUX; www.roc.noaa.gov/WSR88D/Engineering/NEXRADTechInfo.aspx). The specifications for each of the four radars utilized in this study can be found in Table 2. Editing of all these datasets in the National Center for Atmospheric Research's (NCAR's) Solo3 was performed in order to remove any erroneous echoes, ground clutter, as well as unfolding of the velocity data.

3.21 Dual Doppler Analysis

One important component of this project is to conduct a Dual-Doppler synthesis, which will provide quantitative evidence concerning changes in storm intensity in relation to environmental variations and interactions. Each possible combination of radars during their scanning periods was evaluated to assess the location of dual-Doppler lobes (e.g., Fig. 28) and length of availability (Table 3). After removing data of poor quality (described in more detail below), two compatible dual-Doppler combinations were found, providing nearly-continuous coverage of the supercell pair between 0005 UTC and 0048 UTC (Table 4). The two DOWs had a coordinated dual-Doppler deployment from 0005

to 0033 UTC. The two SMART radars also had a dual-Doppler deployment from 0030 to 0248 UTC; however, SMART-R2 had a receiver failure that day. Thus, SMART-R1 was paired with DOW-7 to add coverage for another 15 minutes. Also available for analysis was the National Oceanic and Atmospheric Administration (NOAA) X-POL (NOXP) radar from the National Severe Storms Laboratory (NSSL). However, this dataset had missing data in every other azimuth, so this dataset was also removed from the analysis. Lastly, KPUX WSR-88D data was available throughout the entire period, but no mobile radars ever got within a range suitable for dual-Doppler synthesis to be performed as a result of the storm being too close to the baseline of the radars (e.g., Fig. 29), or insufficient overlap of radar volumes (i.e., KPUX scanning higher than the mobile radars). For the data that has been found suitable for this study, the timeframe between 0005 and 0048 UTC is at least right around the time of the merging of the two cells, so some useful information should still be able to be obtained. However, it should also be noted that, only cell B is consistently within the dual-Doppler lobes, thus it will be the only storm available for analysis during the aforementioned time period.

Before the dual-Doppler synthesis can be performed, the radar data must first be interpolated into a Cartesian grid. Given the differing beam widths of SMART-R1 and the DOWs, each radar will have a Cartesian grid of different dimensions. The DOW data were interpolated onto a 60-km x 60-km grid using a two-pass Barnes analysis scheme (Barnes 1964; Majcen et al. 2008), with a horizontal and vertical grid spacing of 0.25 km. The SMART-R1 was interpolated onto a 150 km x 150 km grid using the same two-pass Barnes analysis scheme, but with a horizontal and vertical grid spacing of 0.5 km to account for the wider beam width in the SMART-R1 data. For all the radar datasets, the

Barnes smoothing parameter κ was set to 1.9 km^2, which remains consistent with the recommendations of Pauley and Wu (1990) and Trapp and Doswell (2000), as well as the work done in Davenport and Parker (2015a). Upon the recommendation by Majcen et al. (2008), a between-pass convergence parameter of $\gamma = 0.3$ was also used. Corrections were also made based upon the storm motion, which is based on the motion of the mesocyclone, and was approximated between each scan of the KPUX radar, following the mesocyclone, or the center point of the storm if a mesocyclone was not present.

Utilizing this objectively-analyzed radar data, dual-Doppler synthesis is performed. A flat lower boundary was used, the height of which was determined by the average elevation of the two radars being synthesized. Upward integration of mass continuity was conducted to focus on the low-level features of interest. Data located within a maximum between beam angle of 30 degrees and a maximum elevation angle of 50 degrees was incorporated into the synthesis.

CHAPTER 4: RESULTS

4.1 Radar Overview

An overview of storm evolution from the perspective of the NWS Pueblo radar (KPUX) is presented in Fig. 30, illustrating the key trends and events of note, as they would have been identified by an operational forecaster. A more detailed description will follow utilizing mobile radars.

Storm initiation occurred near 2033 UTC on 11 June 2009, along a north to south oriented stationary front in eastern Colorado (Fig. 1), just to the southeast of Canon City, Colorado. Over the next hour or so, this nascent storm (hereafter known as Cell A) moved nearly due east, passing just north of Pueblo, CO, quickly gaining intensity as reflected in increasing reflectivity. Cell A took some time to organize and develop clear, consistent supercellular characteristics, but by 2251 UTC, we start to see that transition occur, with a very clear hook echo and some rotation present, which was evident by the cell setting off the mesocyclone detection algorithm (MDA) around 2305 UTC. Next, Cell B forms near the same stationary front as Cell A, due south of Cell A between Pueblo and Ordway, Colorado. Cell B starts to become very organized moving due east, but still not very intense to this point. In the next 20 minutes, between 2305 and 2323 UTC, Cells A and B both undergo a period of intensification, as is evident in increasing reflectivity and Doppler velocities. At 2342 UTC, Cell A and B begin the merger process, as the 40 dBZ reflectivity values for both cells have now merged. At the same time, Cell B grows larger and reaches the inflow region of Cell A. After this Cell A begins to make

a very slight deviation from due east, thus allowing for the merger to take shape. The storms maintain their individual rotating updrafts, however, for some time following this initial merger; these will be referred to as Cell A' and Cell B'. Between 2342 UTC and 12 June 2009 at 0023 UTC, Cells A' and B' continue to merge and appear to strengthen slightly; the details of this trend will be quantified later in this section. Notably, at 0023 UTC, rotation of tornadic strength (i.e., the tornado vortex signature [TVS] algorithm) is indicated in Cell A', which provides further evidence of intensification as a result of this merger. Indeed, increases in intensity following storm mergers are consistent with previous research (Wurman et al. 2007, Rogers and Weiss 2007). The storms continue to merge over the next hour; by 0210 UTC, only a single rotating updraft is present. After 0210 UTC, the cell would continue to move on well into the overnight hours as a discrete supercell, not dissipating until close to 0930 UTC. However, after approximately 0200 UTC, there is a lack of reliable VORTEX2 data to provide storm-scale information, precluding further discussion.

4.2 Environmental Characteristics

As the supercell pair evolved over time, the near-storm environment, both ahead of and behind the storms, also changed over time. Four soundings launched between 2329 UTC and 0202 UTC in the near-inflow environment of the two supercells (Figs. 15-17) will be examined to assess the role of environmental changes in producing the observed storm evolution, with corresponding parameter values. found in Table 5. Additionally, three soundings were launched into the RFD environment (Fig. 24-26) of the supercell pair to evaluate how the cells changed the environment as they passed through the area between 0033 UTC and 0214 UTC. These largely favored the RFD

region behind Cell B, with only the sounding at 0214 UTC centered between, and well behind, the two cells.

4.21 Near Inflow Environment

The initial inflow measurement was collected during the mature stage of both Cell A and Cell B, at 2329 UTC. Accordingly, a moist, unstable environment is present (Fig. 20a), with moderate SBCAPE values of around 1600 J/kg, and a very small -11 J/kg of SBCIN (Table 5). Shear and helicity values in all measured layers are still relatively low at this point as well, which is also evident in the hodograph (Fig. 21a) but are within the typical range to produce non-tornadic supercells (Rasmussen and Blanchard 1998). The supercells began to merge shortly after this initial sounding, though they still had individual updrafts approximately 45 min later, when the next inflow profile was collected. Overall, the 0014 UTC environment was similar, though it was slightly drier throughout the low-levels (Fig. 20b). This low-level drying trend continues at 0058 UTC, which could be due to the fact that this sounding was launched farther south of the storm, so it may not have captured the cirrus deck like the previous two had (Fig. 20c). However, by 0206 UTC, the low-levels significantly cool and moisten, likely associated with the start of the nocturnal transition (Fig. 20d). Accordingly, between 2329 UTC and 0206 UTC there is a significant increase in wind shear, as denoted by large increases in 0-1 km, 0-3 km and effective layer SRH values. One could also easily see this trend by observing the hodographs (Fig. 21), where clockwise curvature increases significantly during the same time period. Consistent with this evolution, both the supercell composite parameter (SCP) and the fixed significant tornado parameter (STP) increase as the evening wears on (Table 5), largely tied to the substantial increase in SRH throughout the

period. Also, from 2329 UTC to 0206 UTC, the depth of the CAPE profile with height significantly decreases, from about 2 km at 2329 UTC, to just under 1 km at 0206 UTC (Fig. 22).

Decreases in CAPE and increases in CIN may at the surface suggest storm weakening or demise; however, the strong increases in SRH through the early evening can promote storm maintenance, as suggested in several previous studies (e.g. Sherburn and Parker 2014, Coffer and Parker 2015, Gropp 2017). Indeed, the supercells are sustained throughout the period, and rotation is evident even after 0200 UTC following the merger (Fig. 30).

4.22 NWS Soundings

In order to depict the environment that the two cells would eventually move into, an additional sounding was selected from the NWS office in Dodge City, KS (Fig. 23). This sounding will be compared to the 00:14 UTC launch from the VORTEX 2 soundings (Fig. 20b, 21b, and Table 5), as it is the closest spatially and temporally. One last thing to note is that not all of the same parameters were computed in the NWS sounding, but in terms of stability and shear, there is enough information that can be compared to get a good idea of the similarities and differences between the soundings.

Not surprisingly, in terms of stability, the DDC sounding was quite similar to the VORTEX2 sounding. We see moderate SBCAPE values in both the 00:14 UTC VORTEX2 (Fig. 20b) and 00:00 UTC DDC (Fig. 23) soundings, with values between 1000 and 1500 J/kg, and there is also very little SBCIN. In terms of shear, the VOREX2 soundings seems to have slightly higher values of SRH at the 0-1 km and slightly higher at the 0-3 km level than that of the DDC sounding. Even so, these values are well within

the range that would support supercells, so the DDC sounding affirms the fact that these storms are moving into a continuously favorable environment.

4.23 RFD Environment

The initial measurement of the RFD environment was collected at around 00:36 UTC, which was a period where both cell A' and B' were in the mature stage of development and in the process of merging into one cell. Additionally, another cell, formed along the gust front of Cell B, was propagating deeper into the RFD air, eventually dissipating (Fig. 31). The 00:36 UTC sounding appears to have been launched in an area of lighter precipitation along the southwest flank of Cell B' (Fig. 24a). As one would expect, this results in a saturated sounding in the mid-levels (Fig. 25a). When compared to the initial inflow environment (Table 5), SBCAPE values are roughly 40% less in the RFD environment (Table 6), which one would expect after the passage of the gust front. Additionally, SBCIN values are substantially larger as well. The big difference that can be seen in this launch is the substantially lower shear values at nearly all levels. Some sort of contamination looks to be present in the data, which can really be seen in the representative hodograph (Fig. 26a), where values appear to be very random when compared to all other hodographs available. This contamination is likely due to the fact that this launch may have occurred just inside the inflow environment, rather than the RFD environment, thus potentially getting caught in an anvil.

The next two soundings were launched much farther within the RFD environment (Fig. 24b-c). Significant cooling in the low levels can be seen when comparing the 0058 UTC (Fig. 20c) inflow sounding to the 0124 UTC RFD sounding (Fig. 25b). Temperatures in the inflow region are approximately 23ºC, while the RFD region surface

temps are around 19ºC. The SBCIN spiked to near -300 J/kg, consistent with the substantial temperature decreases in the low-levels. The same holds true for the 0206 sounding as well, with even a little more of a decrease in SBCAPE and MUCAPE. However, CIN values decrease to around -100 to -150 J/kg depending on which CIN value is examined (Table 6). Vertical CAPE and CIN profiles from the RFD region (Fig. 27) are consistent with the above analysis, indicating weak instability and large CIN, likely leading to the rapid dissipation of the cell in Cell B's RFD region weak instability and large CIN, likely leading to the rapid dissipation of the cell in Cell B's RFD region weak instability and large CIN, likely leading to the rapid dissipation of the cell in Cell B's RFD region.

4.3 Storm Events Timeline

To assess the influence of environmental changes on storm intensity, a timeline is constructed to quantify observed storm evolution (Fig. 32). Utilizing data from the KPUX radar, several metrics were collected, including maximum vertically integrated liquid (VIL) (a measure of how much precipitation and/or hail is present) (Fig. 32a), maximum differential velocity in the low- and mid-levels (a measure of mesocyclone strength) (Fig. 32b), times where the TVS or MDA flags were raised, which was then compared local storm reports (Fig. 32c), and mesocyclone depth (Fig. 32d). Additionally, the distance between the two mesocyclones was tracked in order to determine when the merger became complete (Fig. 32e). Finally, the CAPE, CIN and SRH profiles were also plotted (Fig. 32f) to give a general sense of the environmental changes over time as well.

4.31 Baseline Period (2024 UTC – 2312 UTC)

First, an understanding of how Cells A and B evolved prior to the first sign of the merger between the two cells should be noted, representing a baseline prior to any interactions or known environmental modifications. After the formation of Cell A around 2033 UTC, the maximum VIL increased quickly to just below 50 kg/m^2. Around 2133 UTC, signs of rotation at the mid-levels began to show up. The mid-level mesocyclone strength quickly increased for the first 10 or 15 minutes, maxing out for this time period at around 73 kts at 2137 UTC. Also occurring at this same time is an increase in the maximum VIL to values close to 50 kg/m^2. Through 2312 UTC, which is roughly 30 minutes prior to the 40 dBZ merger, the mid-level mesocyclone strength slowly decreased, at times becoming completely unapparent, and fluctuated between 40-60 kts when visible. At the same time, the maximum VIL values also decreased through about 2300 UTC for Cell A to around 30 kg/m^3 dBZ. Interestingly enough, despite the decrease in mesocyclone strength, the mesocyclone detection algorithm was set off around 2305 UTC, which is a good indicator that the mesocyclone is starting to get more defined. Cell B forms around 2246 UTC and quickly intensifies to max VIL values near 57 kg/m^2 as well by 2309 UTC. As this occurred, Cell B quickly developed a fairly strong mid-level mesocyclone with a value of around 82 kts, followed by a quick decrease to around 50 kts. During the entire baseline period, mesocyclones seemed to remain fairly shallow, only reaching roughly 5-10 km in depth. Cell A had its max values between 2130 UTC and 2210 UTC. During the period between 2130 and 2300 UTC, Cell A produced four severe hail reports. Notably, each hail report coincided with an increase in the mesocyclone strength, and max VIL for Cell A, while Cell B seemed to have hail reports

before VIL was well defined. Also, these hail reports seemed to only occur during a period of time where mesocyclone depth was well-defined, aside from the earliest two reports. So, it will have to be examined farther in this timeline to determine if this will end up being significant or not.

4.32 Pre-Merger Phase (2312 UTC – 0009 UTC)

The pre-merger phase, beginning at 2312 UTC coincides with a sharp increase in mid-level mesocyclone strength for Cell B between 2312 and 2333 UTC; Cell B reached a maximum mid-level mesocyclone strength of 73 kts, with the depth of that mesocyclone jumping significantly, with values around 15-20 kft in depth, with some even higher. However, Cell A undergoes a period of weakening, with the mesocyclone hard to find, if it is there at all. There is a good possibility that this is due to the radar beam undercutting the actual full depth of the mesocyclone, as it passes very close to the radar (Fig. 33). However, by 2351 UTC, mid-level rotation becomes more consistent within Cell A, then quickly jumps in magnitude and depth just prior to the merger at 0009 UTC. Both cells exhibit characteristics here which are consistent with previous research that suggested the period before and just following a merger could be a period of strengthening in supercells (Rogers and Weiss 2007, Wurman et al. 2007, French and Parker 2012). As the merger occurs, the two cells will be renamed Cells A’ and B’ in order to denote that they are now interacting with one another. Also occurring during this period were a few hail reports, with two produced by Cell B and one by Cell A. The two hail reports from Cell B coincide with the time period just after an increase in mid-level mesocyclone strength and VIL in Cell B, while also coinciding with the largest mesocyclone depth measured during the entire period for Cell B. The report associated

with Cell A occurred during a period where data was less reliable, so no significant links were found here.

4.33 Merger Phase (0009 UTC – 0201 UTC)

At around 2342 UTC, as the merger begins, the mid-level mesocyclone strength weakens; yet, a low-level mesocyclone begins to intensify in Cell B', continuing through 0009 UTC, where Cells A' and B' really begin to become one mass of reflectivity. Following this low-level intensification, both Cells A' and B' begin to show increases in mid-level rotation through 0023 UTC, with Cell A' showing the most significant increase. Following this complete merger of reflectivity, more significant fluctuations in intensity occur. The low-level mesocyclone in Cell A' intensified slowly between 0009 UTC and 0047 UTC, reaching a peak intensity of 70 kts around 0047 UTC. In the same time period, cells A' and B' experienced fluctuations in mid-level mesocyclone intensity in both the upward and downward direction.

Between 0047 UTC and 0101 UTC the low-level mesocyclone for Cell A' weakened, eventually dissipating. Cell B' only briefly had a low-level mesocyclone present again. While this occurred, the mid-level mesocyclone strength began to weaken as well for both cells. During this period, there were a total of 4 severe weather reports, with two of those being hail reports from Cell A', one being a hail report from Cell B', and the other being a severe wind report from Cell A'. Notably, an intensifying mid-level mesocyclone again acts as a precursor to the severe reports. The MDA, as well as the tornado vortex signature algorithm (TVS), went off many times during this period, especially between 0038 UTC and 0101 UTC. The TVS was specific to Cell A', with the MDA being specific to Cell B'. After 0101 UTC, the mid-level mesocyclone in Cell B'

weakened rapidly, bottoming out near 24 kts, and remaining that low until around 0200 UTC. The mid-level mesocyclone strength in Cell A', however, remained around 40 kts until 0110 UTC, where it sharply increased to 90 kts again, prompting the TVS to go off again. However, after 0124 UTC, the mid-level mesocyclone strength quickly dropped back to around 40 kts and hovered between that and 60 kts until around 0200 UTC. During this period, there was also a notable decrease in VIL in Cell A' from 62 kg/m^2 at around 0030 UTC down to below 40 kg/m^2 at around 0130 UTC. Interestingly, the large spike in mid-level mesocyclone strength in Cell A' was not matched by an increase in VIL. Also, of note was the note made earlier about potential evidence of the gust front beginning to move out ahead of cell B at 00:47 (Figs. 31f, 32f). With a significant and constant decrease in VIL associated with Cell B, as well as decreases observed in the mid-level mesocyclone strength and depth, it is a safe bet to say that this gust front had at least a temporary weakening effect on Cell B'. By 0201 UTC, the two mesocyclones have finally become one singular mesocyclone (Fig. 32e), so Cells A' and B' are officially merged in all aspects and become Cell C. In this period there were two hail reports from Cell A' and one from Cell B', which again seem to coincide with times either during or just after mid-level mesocyclone intensification, and an increase in VIL.

4.34 Post-Merger Phase (0201 UTC – 0247 UTC)

Lastly, a discussion of how the storms evolved post-merger is necessary to examine how the storms held up just after the actual merger. After 0201 UTC, the mid-level mesocyclone intensity slowly weakened from about 83 kts at 0210 UTC to around 53 kts by 0242 UTC. Following this, another jump up to around 71 kts was observed at around 0247 UTC. Just after this point, another severe hail report comes in around 0247

UTC, again, after a mid-level mesocyclone strengthening phase. This also marks the last point where an accurate mesocyclone depth can be measured. After the merger is complete at 0201 UTC, mesocyclone depth increases by about 5 kft, but then data becomes unusable thanks to range folding of velocity data. After 0247 UTC, the storm began to move into a significant radar gap between the KPUX WSR-88D radar and the WSR-88D radar in Dodge City, KS (KDDC), and we also lose reliable VORTEX2 radar data, so the analysis has to end here. Cell C would continue on tornado warned through around 0230 UTC but would then lose that warning and become only severe warned from 0230 onward through the end of our analysis period here.

4.4 Dual Doppler Analysis

The goal of this project was ultimately to investigate what causes intensity changes in this pair of storms in such a complex environment. A really good way to do that would be to gather updraft intensity and vertical vorticity data from DDA throughout the period when Cell A and Cell B begin merging and continue all the way through the merging process. Unfortunately, with the data issues described earlier on, that was not possible in this case. However, it would seem as though some useful data could be gathered in the period just after the merger begins, which was described in the previous section, and will be used to compare to other radar and environmental data collected later on. Also, due to limitations in the size of the dual-Doppler lobes, as described in section 3.21, only Cell B can be consistently analyzed. Additionally, focus will remain only on the trends in values during this analysis, as values do seem a bit high for all variables at all levels. This is believed to be in response to the vertical integration technique used in objective analysis.

Now, to prove that the cells had already started the merging process, one can clearly observe a linear updraft having already been established by 00:05 UTC at 1 km (Fig. 36a) and 3 km (Fig. 37a). This feature is likely the gust front from Cell A acting as an extra forcing mechanism on Cell B. Maybe this helped to bridge the gap between the two cells and started to merger process in the first place. These comparisons cannot be made precisely since we don't have data before the merger but would be an interesting topic to look into in further studies similar to this, but with a larger field of available data. Looking at the rest of the analysis period, the linear updraft feature remains in sight throughout the period of analysis at 1 km (Fig. 36) and 3 km (Fig. 37). By the end of the analysis, there may be some evidence showing that this gust front is trying to push out ahead of the storm. Perhaps looking at KPUX radar data beyond this point can show some insight into whether the storm begins weakening later on. That data will be discussed in a farther section and compared to what was seen here in the DDA.

4.41 Trends in Updraft Intensity and Area

The first task in the dual-Doppler analysis was to analyze the intensity of updrafts within the cells, which will help to better quantify strengthening and weakening phases during the lifetime of these cells. This was done by computing maximum updraft strength at two vertical levels (1 km and 3 km). As shown in Fig. 34, the 1 km maximum updraft speed was fairly steady throughout the analysis period, with a couple of peaks around 00:12 UTC and 00:28 UTC. However, the 3 km maximum updraft speed exhibited more significant variation, with a fairly steady increase through 00:20 UTC, then when data returns at 00:40 UTC, values are much lower again. When looking back at Hastings and Richardson (2016), there was a case that very closely mirrored the case in the present

study, which I believe can partially explain this increase following the merger. With a cold pool obviously present in the 11-12 June 2009 case, Fig. 8b shows a similar example to the present study. The results stated that when the stronger northern cell merges with a weaker southern cell, the northern cell will take over and turn into a high precipitation supercell. This is exactly what appears to happen in the present study (Fig. 27). Also, recall the broad conclusion from this study, which was that rear flank mergers result in stronger mesocyclones (by 300-400%), meaning that cells that merge in the rear flank tended to gain strength. This increase in mesocyclone strength is also observed in the present study, which can be easily seen in both the radar timeline (Fig. 30), where brighter colors show up gradually after the merger in both reflectivity and velocity, and also in the graphed data itself in the storm events timeline (Fig. 32b). Though we don't have enough dual-Doppler data to examine anything past 00:47 UTC, just looking at the KPUX radar data timeline shows that this was a very similar case. Additional data would be needed to determine if the updraft strength continued this upward trend or not though. Additionally, Wurman et al. (2007) performed a case study of merging cells on tornadogenesis, where two different mergers occurred (Fig. 8). Utilizing dual-Doppler analysis to examine the 3D wind field, it was revealed that short-lived tornadoes immediately resulted from each merger; however, the storm quickly weakened after that point. The present study did not observe a tornado, however tornadoes form as a result of significant vertical stretching, indicating a very strong and intensifying low-level updraft. So, if you take that into account, you see a quick increase in updraft strength at 3 km between 00:05 UTC and 00:20 UTC (Fig. 30), followed by a period of missing data, then

values that have weakened significantly. So, this would be somewhat consistent with the results from Wurman et al. (2007).

After assessing the maximum updraft strength, it is also useful to get an idea of updraft size, which can be another measure of intensity change. Remaining consistent with updraft intensity, this updraft area was calculated at both the 1 km and 3 km levels, and those time series can be seen in Fig. 35. At the 1 km level, updraft area maxed out around 00:10 UTC, before remaining steady through 00:28 UTC, then steadily dropping back down through 00:32 UTC. The same trend was also observed at the 3 km, however, the updraft area increased through 00:16 UTC before dropping down again.

4.42 Trends in Vertical Vorticity Strength and Area

The broad trends in vertical vorticity largely mirrored those identified with the updraft strength and size. Maximum vertical vorticity was generally quite variable at both 1 and 3 km. Interestingly, a notable spike at both levels was evident near 00:40 UTC, but then quickly weakened again, perhaps in response to vertical stretching due to strengthening of the 3 km updraft (Fig. 34). Next, using a threshold of $0.01s^{-1}$, trends in the size of rotation are very similar in nature to that of the updraft, with a peak at around 00:14 UTC (1 km) or 00:16 UTC (3 km) before steadily dropping through the end of the period.

CHAPTER 5: SUMMARY AND FUTURE WORK

The amount of data available during the 11-12 June 2009 supercell pair in southeastern Colorado provided a unique opportunity to closely examine the life cycle of a pair of supercell thunderstorms that underwent a merger while simultaneously undergoing the nocturnal transition, wherein a HSLC environment began to set up. Both cells A and B intensified quite rapidly (Fig. 30) after being initiated along a stationary front draped north to south across eastern Colorado (Fig.1). As the pair of supercells evolved, four inflow soundings were collected, illustrating significant increases in SRH and CIN, as well as a decrease in CAPE (Figs. 20-21, Table 5). Then, there were also three soundings within the RFD region, which showed insufficient CAPE and large amounts of CIN (Figs 25-26, Table 6), which indicates that storms would struggle to maintain themselves in this environment. This becomes significant in later portions of the storm, where the gust front is thought to advance far enough into the inflow environment of Cell B' to cause changes in intensity. To analyze the results of the study thus far, conclusions are broken up into four sections, similar to what was done in the events timeline, focusing on times relative to the merger of the two supercells.

5.1 Baseline Period (2033 UTC – 2312 UTC)

In the baseline period, the analysis focused on data from the WSR-88D radar in Pueblo, CO, so the results from the timeline analysis will be the focal point, along with the closest sounding to the end of the time period, which was launched at 2329 UTC. Within a moist and unstable environment and sufficient deep-layer shear (e.g., Fig. 20a;

Table 5), the mid-level mesocyclone strength consistently remained between 40-60 kts for Cell A, while Cell B seemed to be a bit stronger initially as it was forming, and seemed to strengthen quicker than Cell A did in relation to the time that the cell formed, and the time the cell gained some mid-level rotation (Fig. 32b). The interesting thing to note in this timeframe was the relationship between severe hail reports and mesocyclone strengthening phases. There is a correlation between any amount of strengthening in the mid-level cyclone and a hail report occurring shortly afterwards.

5.2 Pre-Merger Phase (2312 UTC – 2342 UTC)

Moving into the pre-merger phase, one can clearly observe from Fig. 32b that the mid-level mesocyclone strength started to experience much more intense fluctuations in strength, reaching strengths as high as 80+ kts in both cells, and even reaching low strengths of near 35 (40) kts for Cell A (B). So, it is quite clear that the merger of these two cells changes something in the storms. There continues to be a relationship between hail reports and mid-level mesocyclone strength. Given the short period of this phase, it is assumed that environmental variability played little role in the observed storm fluctuations.

5.3 Merger Phase (2342 UTC – 0201 UTC)

During the merger phase itself, again it is obvious from Fig. 32b that the intensity fluctuations are much more intense within this period than in the baseline period earlier on. There are several other interesting things of note in this period, led by the continuation of the relationship between severe reports and mid-level mesocyclone intensification phases, so that will be something to look deeper into in later parts of the analysis for sure, as consistent as it has been throughout different phases of this storm.

The TVS and MDA algorithms were both set off multiple times, primarily between 0030 UTC and 0130 UTC, so this indicates that the rotation is not only strong, but likely deep and consistent. Notably, this phase is also associated with the nocturnal transition; accordingly, a decrease in instability, increase in inhibition, and strong increases in SRH were observed (Fig. 20b, c, d; Table 5). Given the maintenance of the merged storm, as well as the near-continuous presence of a TVS signature, it appears that the increases in SRH were sufficient to produce strong dynamical lifting in spite of the increasingly weak instability.

5.31 Dual-Doppler Analysis on Cell B/B'

Focusing on the evolution in Cell B via dual-Doppler analysis between ~00:05 and 00:50 UTC, there were similar trends in both the updraft and vertical vorticity. The maxima in each were quite variable; the most notable trends occurred at 3 km, where an upward trend was present in the maximum updraft through about 00:20 UTC, which was then proceeded by a spike in 3 km vertical vorticity near 00:39 UTC, indicative of stretching (Fig. 34). It is difficult to tease out just how much of the noisy trends are a result of the merging process or the environmental changes. While the instability of the near-storm environment was observed to weaken between 00:14 and 00:56 UTC, the low-level SRH notably strengthened (Table 5). So, it is possible that the increase in updraft strength was a result of stronger dynamical lifting, but may also be a function of the merger itself.

5.4 Post-Merger Phase (0201 UTC – 0247 UTC)

After the merger occurs, there is unfortunately no accompanying VORTEX2 data. What is available from KPUX demonstrates an uptick in mid-level mesocyclone

intensity, along with a severe hail report at 02:50 UTC. Given the very strong increases in low-level SRH combined with sufficient elevated instability (Table 5), it is no surprise that the storm continues to be maintained.

5.5 Overall Trends

Overall, the fluctuations during and after the merger begins to occur were more intense, compared to those before the merger occurred. This could be linked to the merger itself, but is likely, in large part, due to the substantial increase in SRH values in all measured layers (Table 5), as shown in the increased clockwise curvature in the hodographs (Fig. 21). Another finding from this timeline is the linkage to increased mid-level mesocyclone strength and depth and LSR's. In almost every LSR occurrence, there was an increase in rotation at the mid-levels just prior to the report. This makes some sense, given that the rotation is somewhat indicative of increased updraft strength, which will be quantified later in this study using dual-Doppler analysis techniques. Lastly, as consistent with previous research, the period just following the beginning of the merger seemed to be an inflection point that marked a significant increase in mesocyclone strength at all levels (Fig. 32b). During the merger period, there are several instances of low-level rotation as well, which also would tend to indicate some strengthening, since rotation was able to extend down towards the surface. Dual-Doppler data seemed to only affirm these trends, as most trends in updraft strength seemed to be consistent with that of mesocyclone intensity and depth.

5.6 Future Work

The present study provides only a small sample of analyzing a storms environment in order to determine what contributes to intensity changes within

supercells. Several different environmental characteristics were examined in relation to intensity changes for this pair of supercells (e.g. storm merging, nocturnal transition, changes in the inflow environment, etc.). With this being only one small case study, it would be useful to see if any of the trends observed in the present study translate to other storms in similar environments. Though there are a few studies that go into detail about supercells merging with supercells, they are not nearly as numerous as studies done on supercells merging with other types of convection. This still leaves a gap to be filled in this type of research. Additionally, it would be useful to perform idealized simulations to identify whether the merging process or the shifts in the near-storm environment played a more important role in the overall strength and evolution of this particular event.

TABLE 1: Taken from Davenport and Parker (2015a), their table 1. Table of shear and helicity parameters for observed near-inflow soundings on 9 Jun 2009.

	2319 UTC	2354 UTC	0056 UTC
0–6-km shear ($m\,s^{-1}$)/direction (°)	32.0/257	29.0/264	24.2/247
0–3-km shear ($m\,s^{-1}$)/direction (°)	14.8/247	17.7/237	20.0/251
0–1-km shear ($m\,s^{-1}$)/direction (°)	1.8/241	5.7/236	5.9/215
0–0.5-km shear ($m\,s^{-1}$)/direction (°)	3.2/74	5.4/36	8.0/14
0–3-km EH ($m^2\,s^{-2}$)	136	60	36
0–3-km SRH ($m^2\,s^{-2}$)	319	277	124
0–1-km EH ($m^2\,s^{-2}$)	29	−1	−68
0–1-km SRH ($m^2\,s^{-2}$)	47	53	−7
KDDC storm motion ($m\,s^{-1}$)/direction (°)	12.4/295	14.4/277	11.8/278
Effective layer depth (m)	2120	2130	1910
Effective shear ($m\,s^{-1}$)/direction (°)	18.7/231	19.5/227	11.2/250
Effective SRH ($m^2\,s^{-2}$)	273	215	68

TABLE 2: This table contains some of the more important characteristics for each of the radars used for this study.

	DOW-6 and DOW-7	**SMART-R1**	**KPUX**
Wavelength	3 cm (X-band)	5 cm (C-Band)	10 cm (S-band)
Beam Width	0.9º	1.5º	0.925º
Pulse Repetition Frequency	500-6000 Hz	500-5000 Hz	318-1304 Hz
Maximum Range	45-50 km	90-95 km	230 km (VEL) 460 km (REF)
Transmitter	Mag 2 x 250 kW	250 kW	700 kW
Elevation Angles Scanned	0.5-18º	0.5-38º	0.5-19.5º
Elapsed Time for each Volume	~2 min	~2 min 30 s	~4-5 min

TABLE 3: All dual-Doppler pairs available prior to elimination of bad data.

Dual-Doppler Pair	**Times Available**
DOW-6 (deployment1) & DOW-7 (deployment1)	0005 – 0033 UTC
DOW-7 (deployment 1) & SMART-R1	0038 – 0049 UTC
SMART-R1 & NOXP (deployment 1)	0047 – 0110 UTC
KPUX & NOXP (deployment 1)	0110 – 0130 UTC
SMART-R1 & KPUX	0124 – 0230 UTC
KPUX & NOXP (deployment 2)	0140 – 0207 UTC
SMART-R1 & NOXP (deployment 2)	0156 – 0224 UTC
DOW-6 (deployment 2) & DOW-7 (deployment 4)	0238 – 0300 UTC

TABLE 4: A quick representation of the two dual-Doppler timeframes that were found to be usable for this study.

Dual-Doppler Pair	**Times Available**
DOW-6 (deployment1) & DOW-7 (deployment1)	0005 – 0033 UTC
DOW-7 (deployment 1) & SMART-R1	0038 – 0049 UTC

TABLE 5: Some key convective parameters from the soundings in the near-inflow region of the pair of supercells, as calculated by the SHARPpy soundings.

	Time (UTC)			
Severe Parameters	**23:29**	**00:14**	**00:56**	**02:06**
0-1 km SRH (m^2/s^2)	60	117	199	410
0-1 km Shear (kts)	6	15	14	17
0-3 km SRH (m^2/s^2)	129	163	225	461
0-3 km Shear (kts)	19	25	26	33
0-6 km Shear (kts)	26	31	36	31
DCAPE (J/kg)	753	1033	1012	718
EBWD (kts)	15	24	22	20
Effective SRH (m^2/s^2)	114	135	210	426
MLCAPE (J/kg)	473	0	26	67
MLCIN (J/kg)	-47	0	0	0
MLLCL (m AGL)	2238	6270	10267	10954
MLLI (Degrees Celsius)	-2	-1	-6	-4
MUCAPE (J/kg)	1599	1577	1233	1008
MUCIN (J/kg)	-11	-56	-108	-71
MULCL (m AGL)	1306	1254	1662	684
MULFC (m AGL)	2117	2159	2497	2294
MULI (Degrees Celsius)	-5	-7	-7	-3
SBCAPE (J/kg)	1599	1577	1233	943
SBCIN (J/kg)	-11	-56	-108	-87
SBLCL (m AGL)	1306	1254	1662	599
SBLFC (m AGL)	2117	2159	2497	2297
SBLI (Degrees Celsius)	-5	-7	-7	-3
SHERBE	0.6	1.0	1.0	0.6
SHERBS3	0.7	1.0	1.2	1.0
Supercell Composite	2.8	4.3	5.2	8.6
Sig. Hail Parameter	0.5	0.8	0.7	0.2
STP (cin)	0.0	0.0	0.0	0.0
STP (fix)	0.4	0.9	0.6	2.6
PWAT (in)	1.07	0.96	0.81	0.88

TABLE 6: As in table 5, but for soundings collected from the RFD region.

	Time (UTC)		
Severe Parameters	**00:36**	**01:24**	**02:06**
0-1 km SRH (m^2/s^2)	20	37	36
0-1 km Shear (kts)	6	8	6
0-3 km SRH (m^2/s^2)	12	145	173
0-3 km Shear (kts)	23	26	23
0-6 km Shear (kts)	8	21	16
DCAPE (J/kg)	966	1015	706
EBWD (kts)	15	27	17
Effective SRH (m^2/s^2)	-30	166	134
MLCAPE (J/kg)	0	1063	480
MLCIN (J/kg)	0	-147	-148
MLLCL (m AGL)	7337	1399	1055
MLLI (Degrees Celsius)	1	-4	-3
MUCAPE (J/kg)	984	1369	788
MUCIN (J/kg)	-84	-90	-113
MULCL (m AGL)	1851	1566	898
MULFC (m AGL)	2256	2593	2629
MULI (Degrees Celsius)	-3	-5	-4
SBCAPE (J/kg)	984	878	782
SBCIN (J/kg)	-81	-278	-149
SBLCL (m AGL)	1851	590	357
SBLFC (m AGL)	2256	2866	2629
SBLI (Degrees Celsius)	-3	-4	-4
SHERBE	0.5	4.6	0.5
SHERBS3	0.8	0.8	0.7
Supercell Composite	-0.5	0.8	1.8
Sig. Hail Parameter	0.1	0.4	0.1
STP (cin)	0.0	0.2	0.1
STP (fix)	0.0	0.2	0.1
PWAT (in)	0.94	0.87	0.99

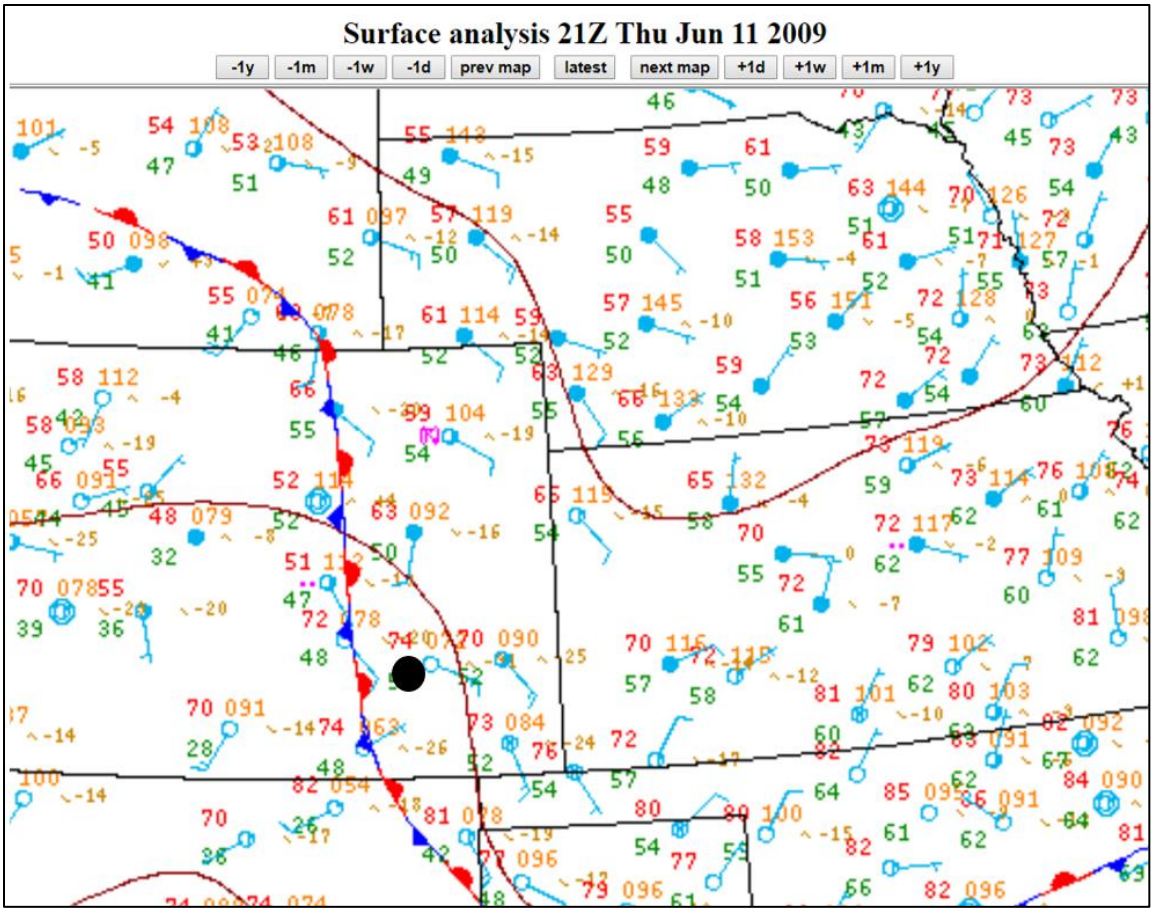

FIGURE 1: Surface analysis from the Weather Prediction Center (WPC) on 11 June 2009 at 2100 UTC. The black dot denotes the approximate location of the area where the parent supercell (Cell A) formed.

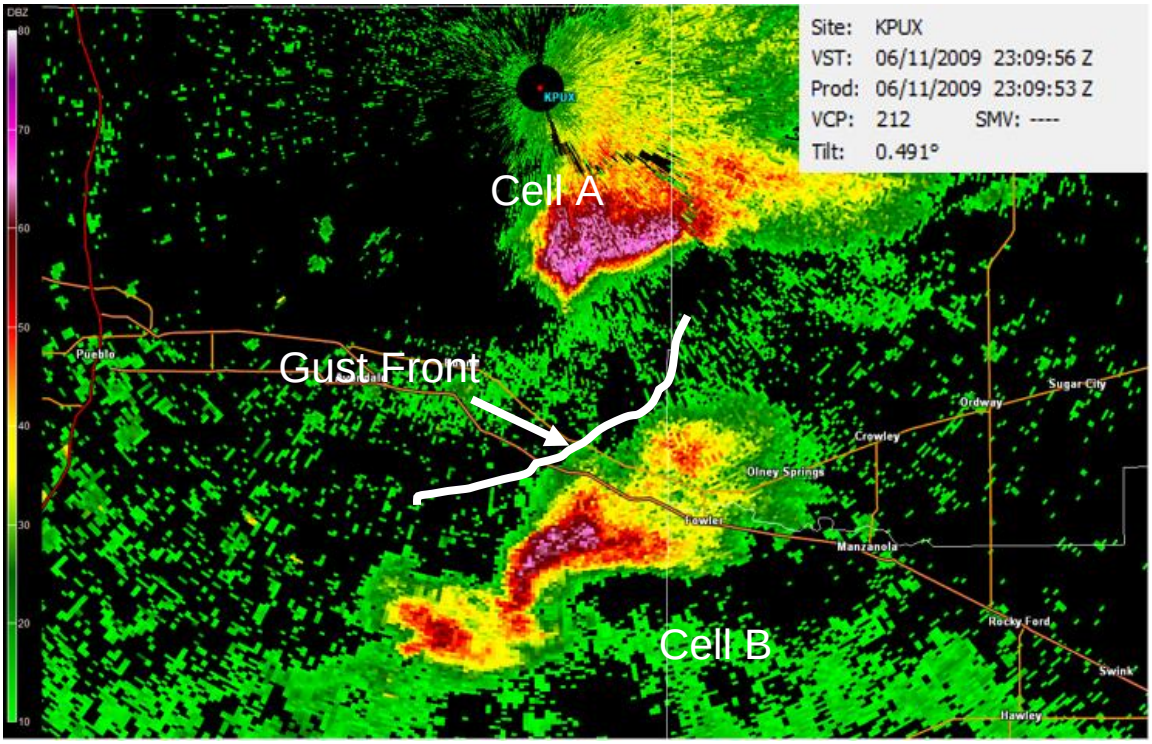

FIGURE 2: Base reflectivity from KPUX on 11 June 2009 at ~2310 UTC. The supercells of interest are labeled, as well as the approximate gust front location associated with Cell A.

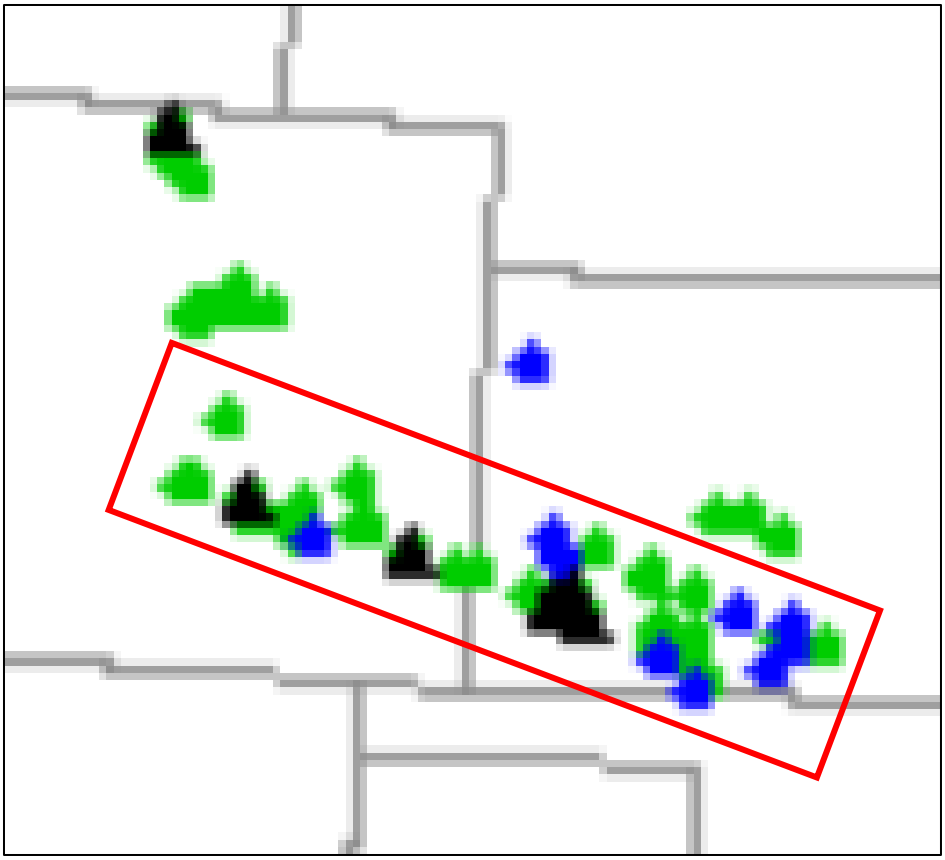

FIGURE 3: Local storm reports from 11 June 2009, with the reports associated with the cells in the study boxed in red. Green dots are hail reports >1 inch in diameter, blue dots are wind reports >58 mph, and black triangles are hail reports >2 inches in diameter.

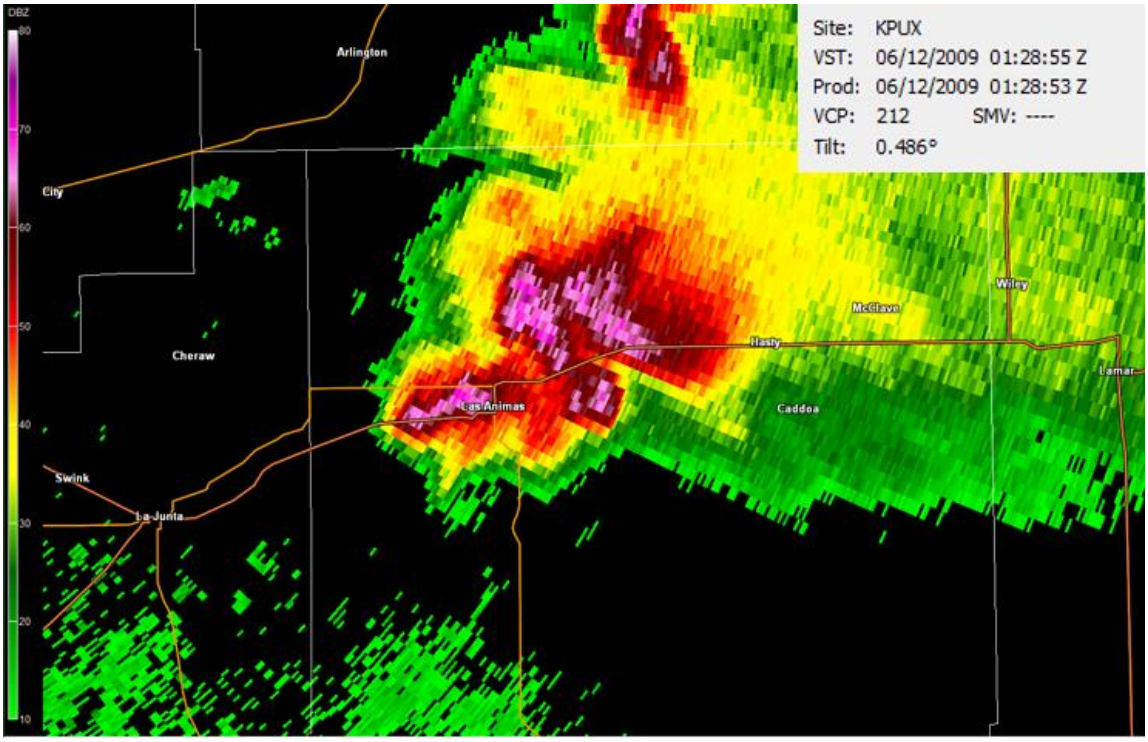

FIGURE 4: Base reflectivity from KPUX on 11 June 2009 at ~0128 UTC showing cells A and B merged into one mass (Cell C).

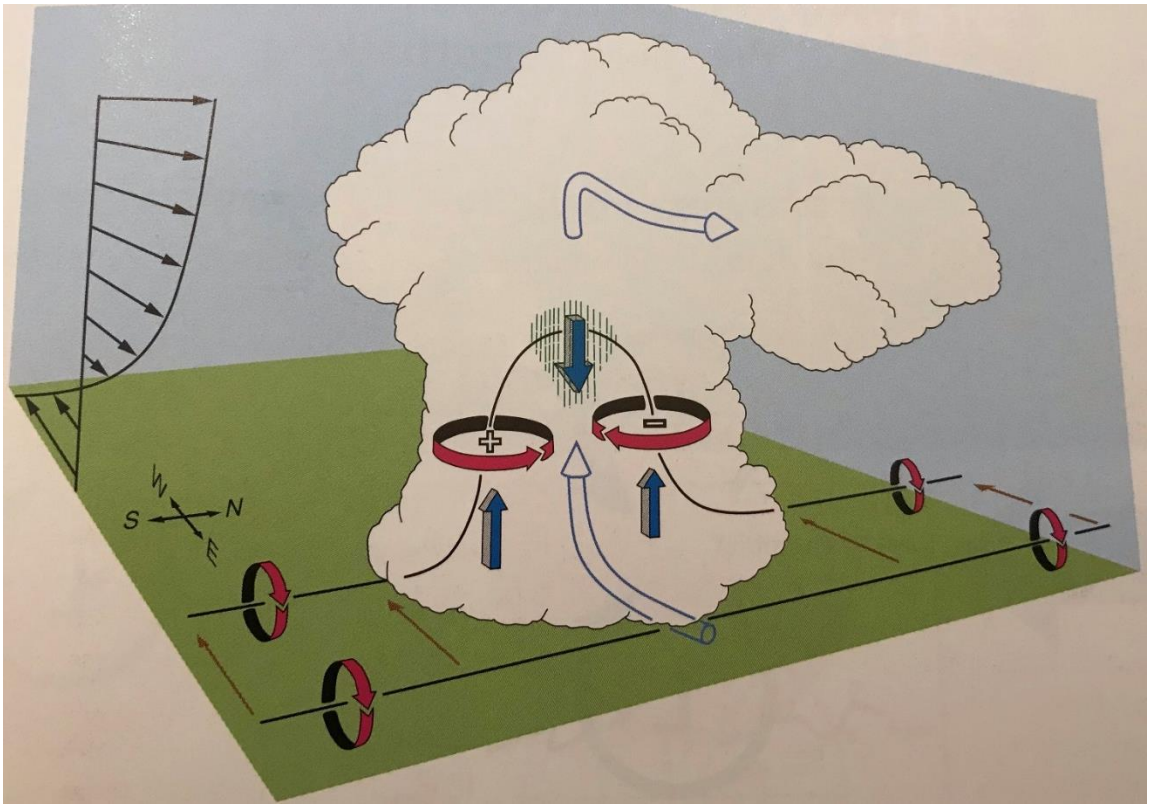

FIGURE 5: Taken from Markowski and Richardson (2013), their figure 8.35a. In the early stage of supercell formation, a vortex pair forms in the mid-levels due to the tilting, by way of updrafts, of horizontal vorticity, associated with vertical wind shear.

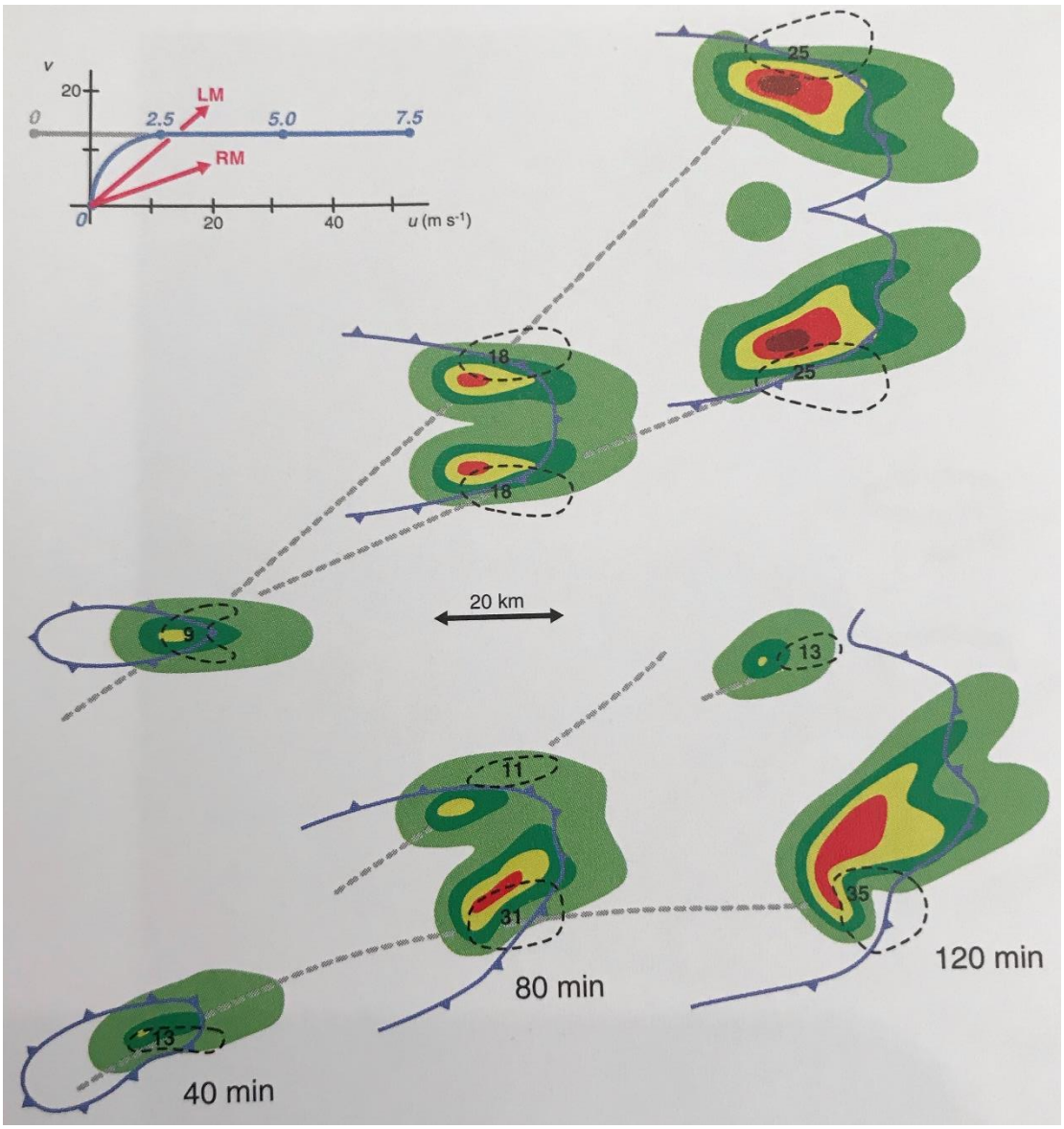

FIGURE 6: Taken from Markowski and Richardson (2013), their figure 8.41. Plan views of cloud-model produced, low-level rainwater fields for two simulations using a straight hodograph (top) in the lowest 2.5k (grey line in hodograph on top left), and a clockwise hodograph (bottom) in the lowest 2.5km (blue line in hodograph on top left). The straight hodograph produces splitting mirrored supercells, while the curved hodograph produces one dominant supercell on the right side, relative to storm motion. Shaded colors represent simulated reflectivity, blue lines with triangles represent gust fronts, dashed black lines represent updraft regions, and dashed grey lines represent storm tracks.

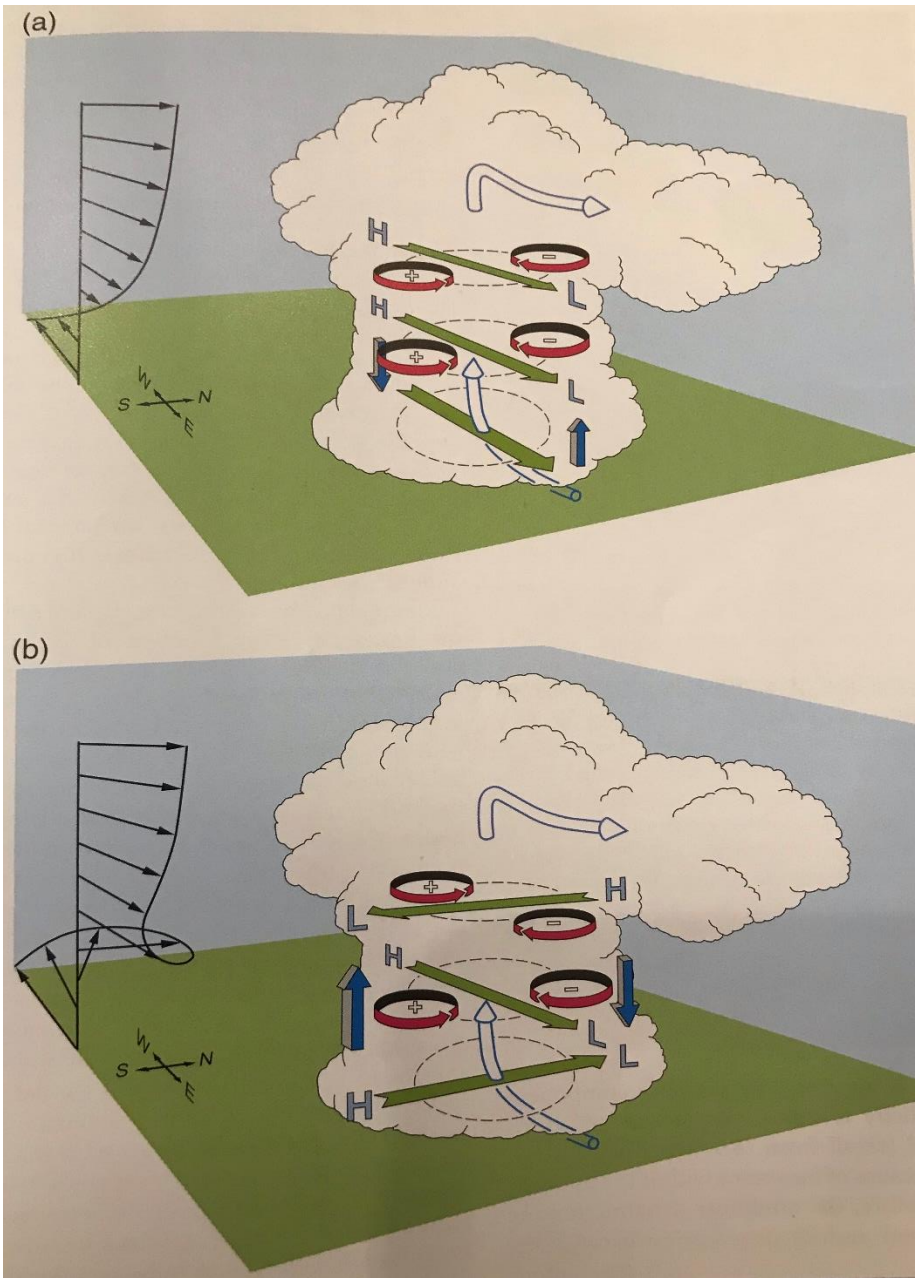

FIGURE 7: Taken from Markowski and Richardson (2013), their figure 8.40. Pressure perturbations resulting from an updraft interacting with vertical wind shear a) that does not change direction with height and b) turns clockwise with height. Dark blue arrows indicate the VPPGF, while green arrows show horizontal PGF.

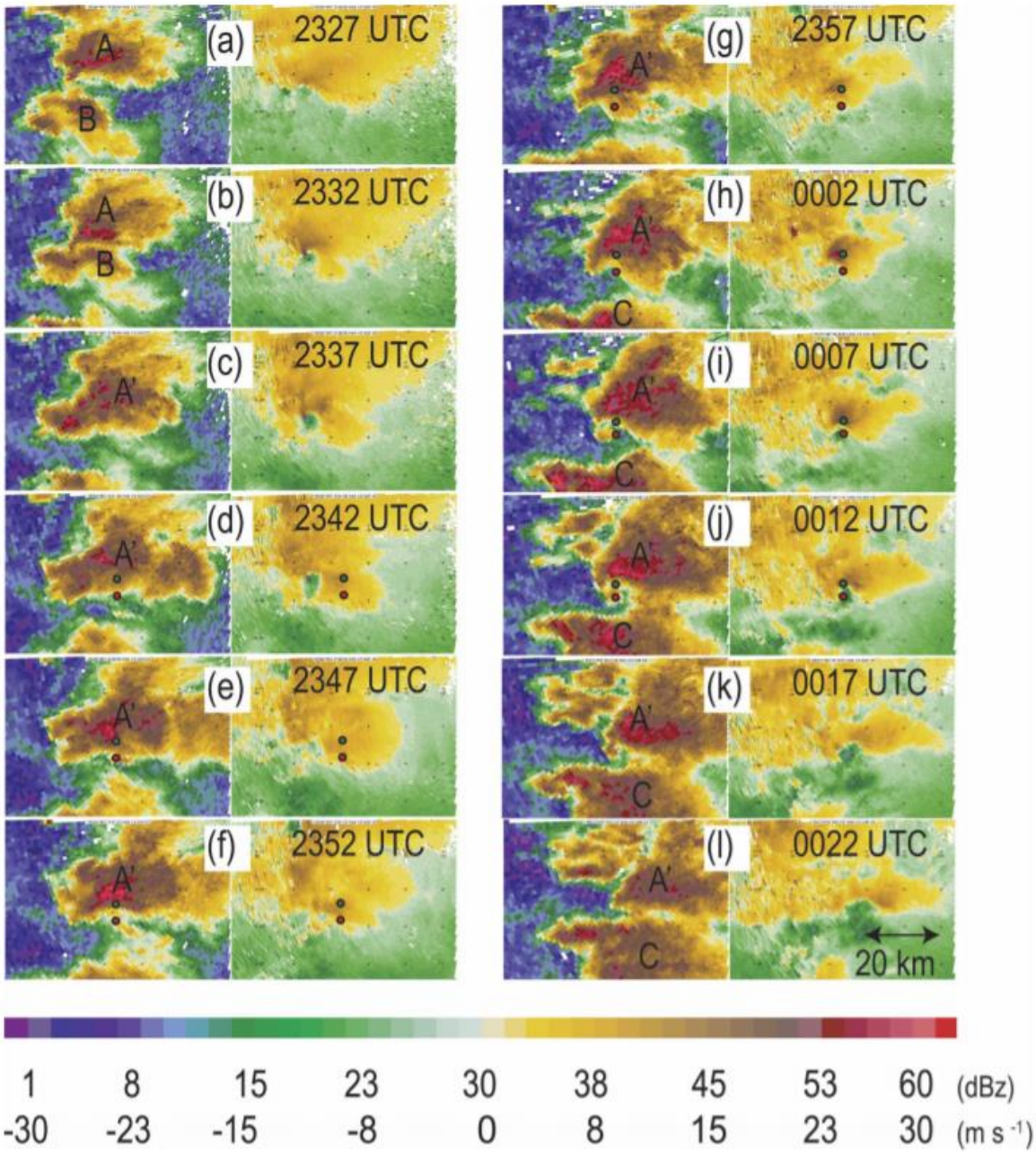

FIGURE 8: Taken from Wurman et al. (2007), their Fig. 3. The 0.5° elevation scan of convective storms A, B, A, and C from KINX (located just off the upper-right corner) showing (left) base reflectivity and (right) Doppler velocity at several times during the evolution of the tornadoes near Kiefer and Glenpool, OK. The locations of DOW2 (red circle) and DOW3 (green circle) are shown.

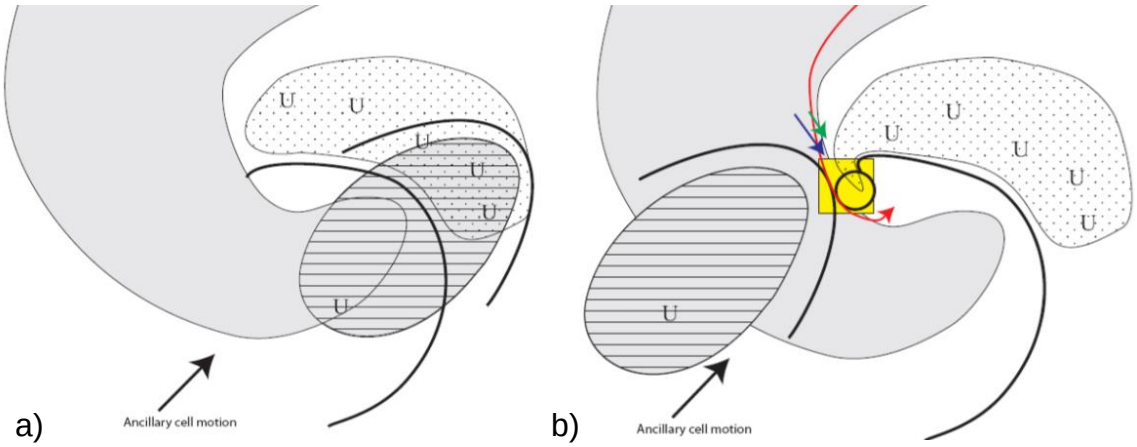

FIGURE 9: Taken from Rogers and Weiss (2007), their Figs. 6-7. a) A schematic diagram of the typical ancillary cell position for null cases within the hook echo region of the primary cell. The solid black lines represent gust fronts. The shaded grey areas represent radar echoes. The striped black region represents the precipitation from the ancillary cell. The dotted region represents the updraft of the primary cell. "U" represents the general area of the updraft in the ancillary and primary cells. b) A schematic diagram of the typical ancillary cell position for tornadic cases within the hook echo region of the primary cell. The red line represents the typical trajectory of air parcels entering the low-level mesocyclone. The black circle represents possible tornado location. Approximate vorticity vectors prior to (green arrow) and after (blue arrow) baroclinic enhancement of horizontal vorticity are displayed. The shaded yellow region is an area of enhanced convergence.

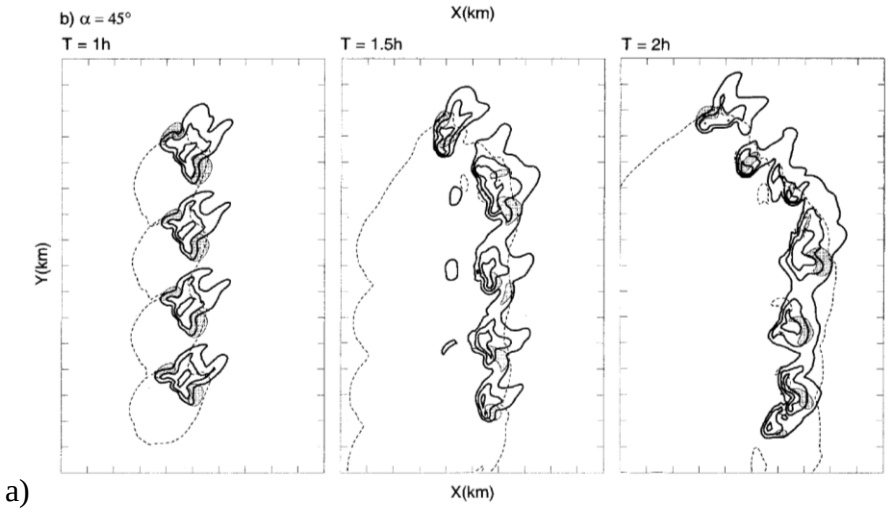

a)

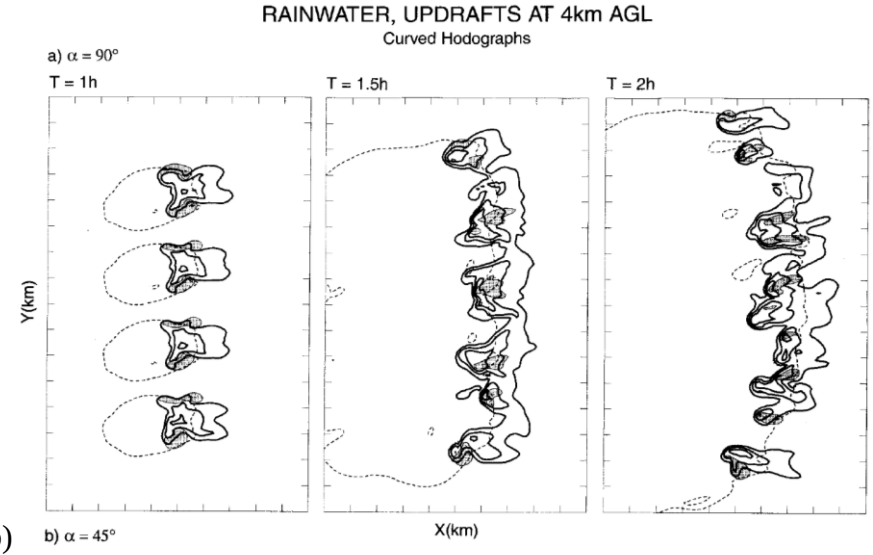

b)

FIGURE 10: Taken from Bluestein and Weisman (2000), their figure 8a-8b. Simulated fields for an isolated thermal bubble, at 1, 1.5, and 2 h, of liquid-water mixing ratio (thick contours at 1, 4, and 8 g/kg) and vertical velocity (shaded region in excess of 8 m/s) at 4 km for the modified sounding and curved hodograph. Tick marksare spaced 10 km apart. Gust front at 0.25 km depicted by dashed line (perturbation temperature at 0.25 km, with respect to ambient environment, of 21ºC). Only a 60 km x 80 km portion of the full domain is shown. Where a) represents the simulaiton run with shear at a 45º to the line of cells and the, and b) represents the line simulation when the shear was at 90º orientation to the line of cells.

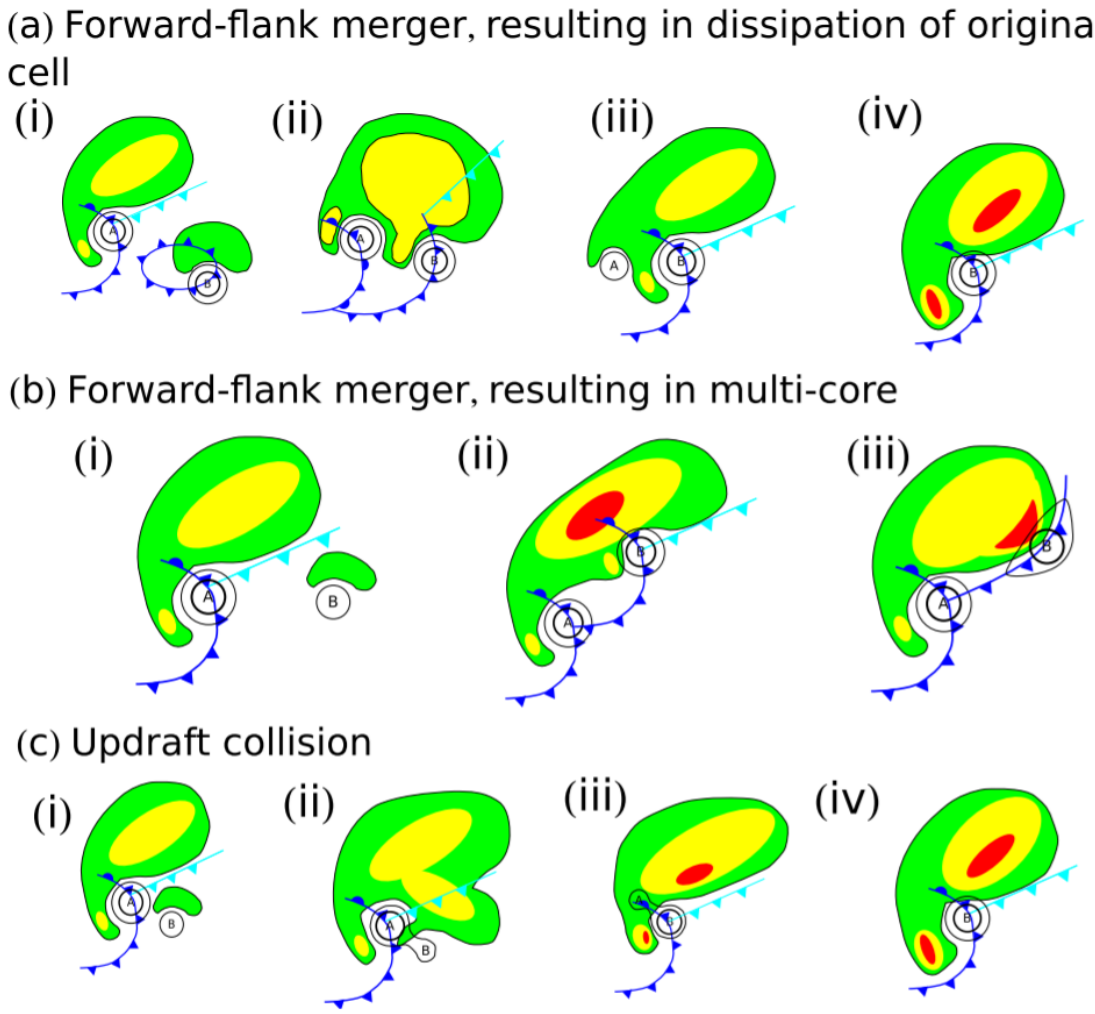

FIGURE 11: Taken from Hastings and Richardson (2016), their Fig. 27. Conceptual models for three types of mergers: a) Forward-flank merger, resulting in multicell system; b) Forward-flank merger, resulting in dissipation of original cell; c) Updraft–updraft collision.

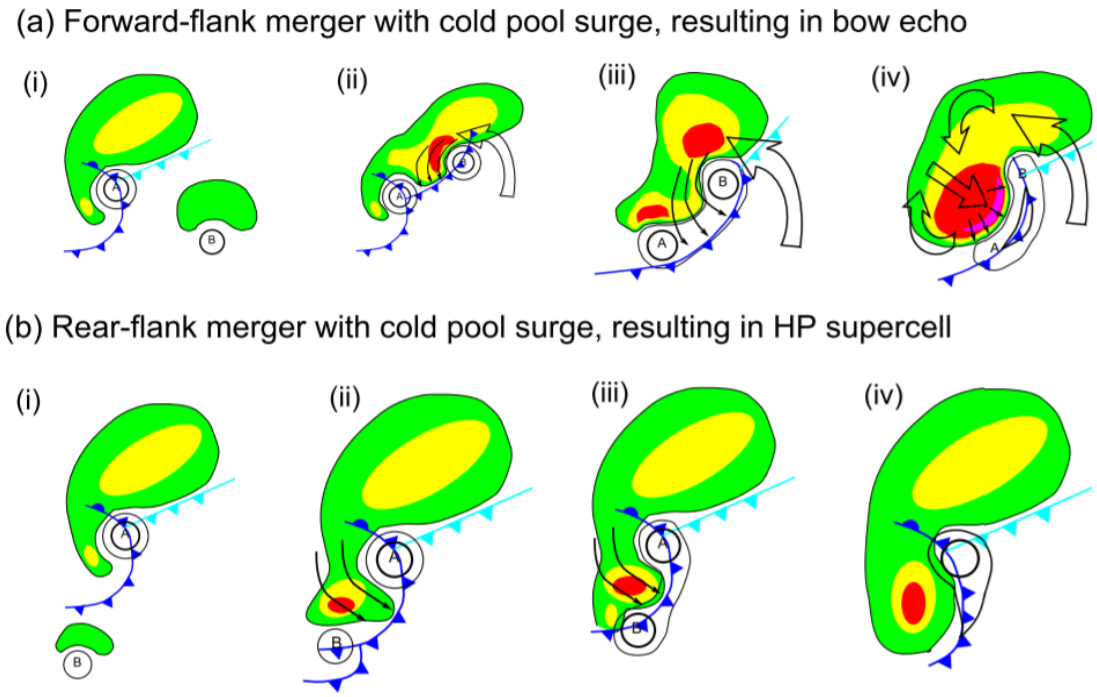

FIGURE 12: Taken from Hastings and Richardson (2016), their Fig. 28. Conceptual models for mergers involving cold pool surges: a) Forward-flank merger resulting in a bow echo; b) Rear-flank merger resulting in a high precipitation supercell.

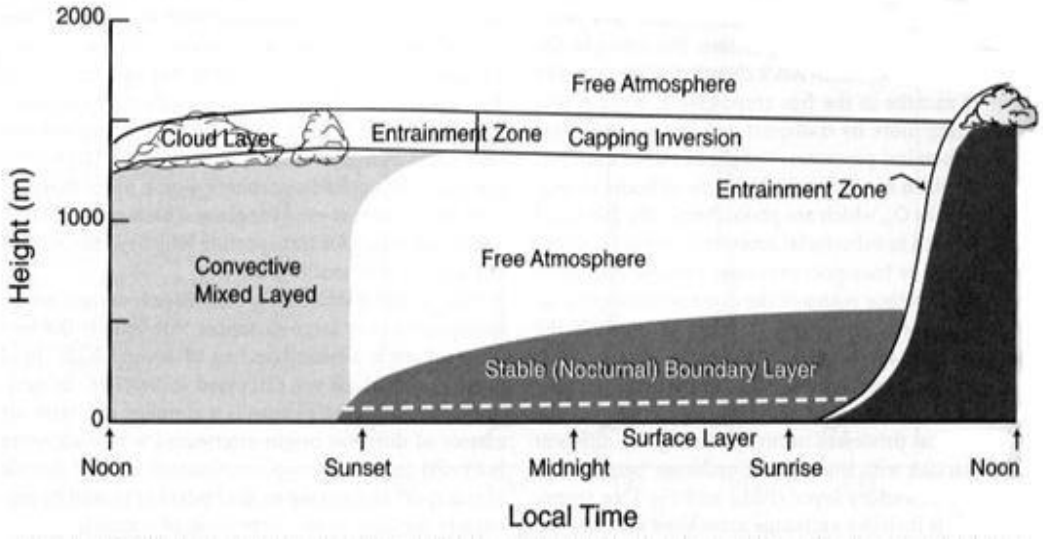

FIGURE 13: Taken from Stull (1988). Diurnal Variation in the structure of the boundary layer.

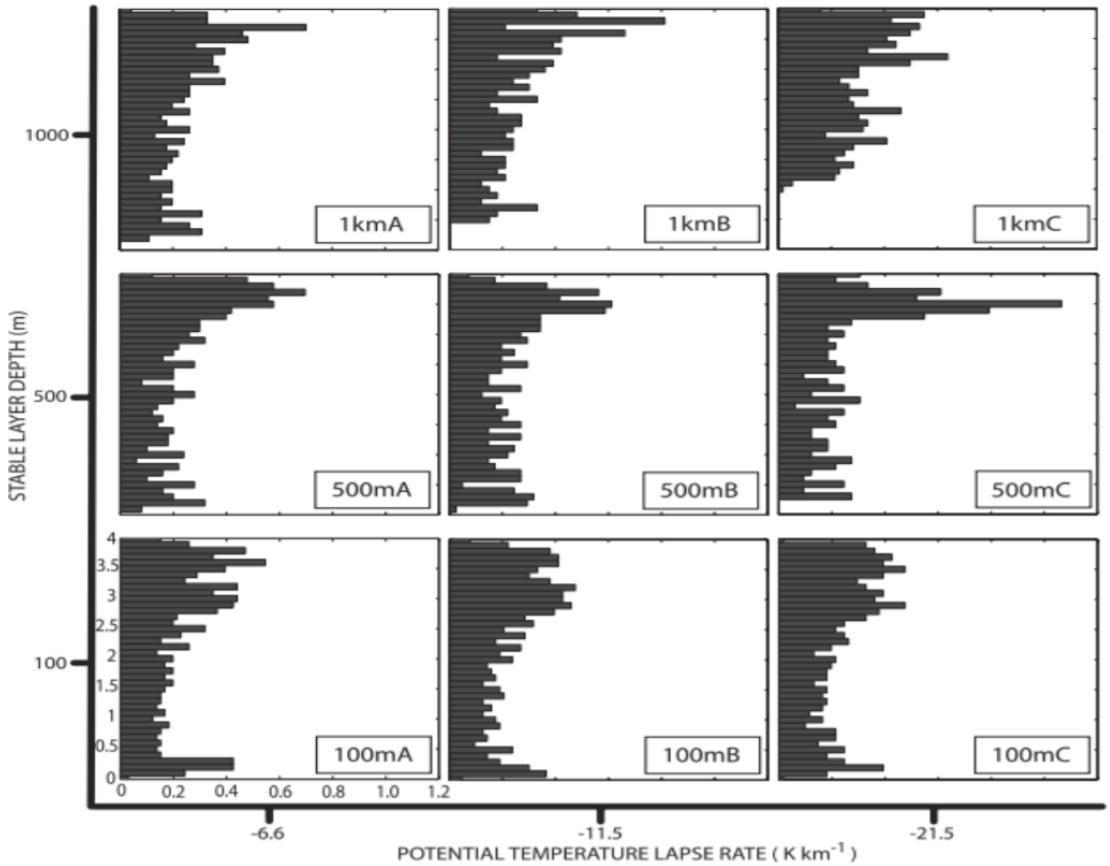

FIGURE 14: Taken from Nowatarski et al. (2011), their figure 13. Normalized histograms of 4-km updraft parcel origin altitude (km) for stable layer simulations.

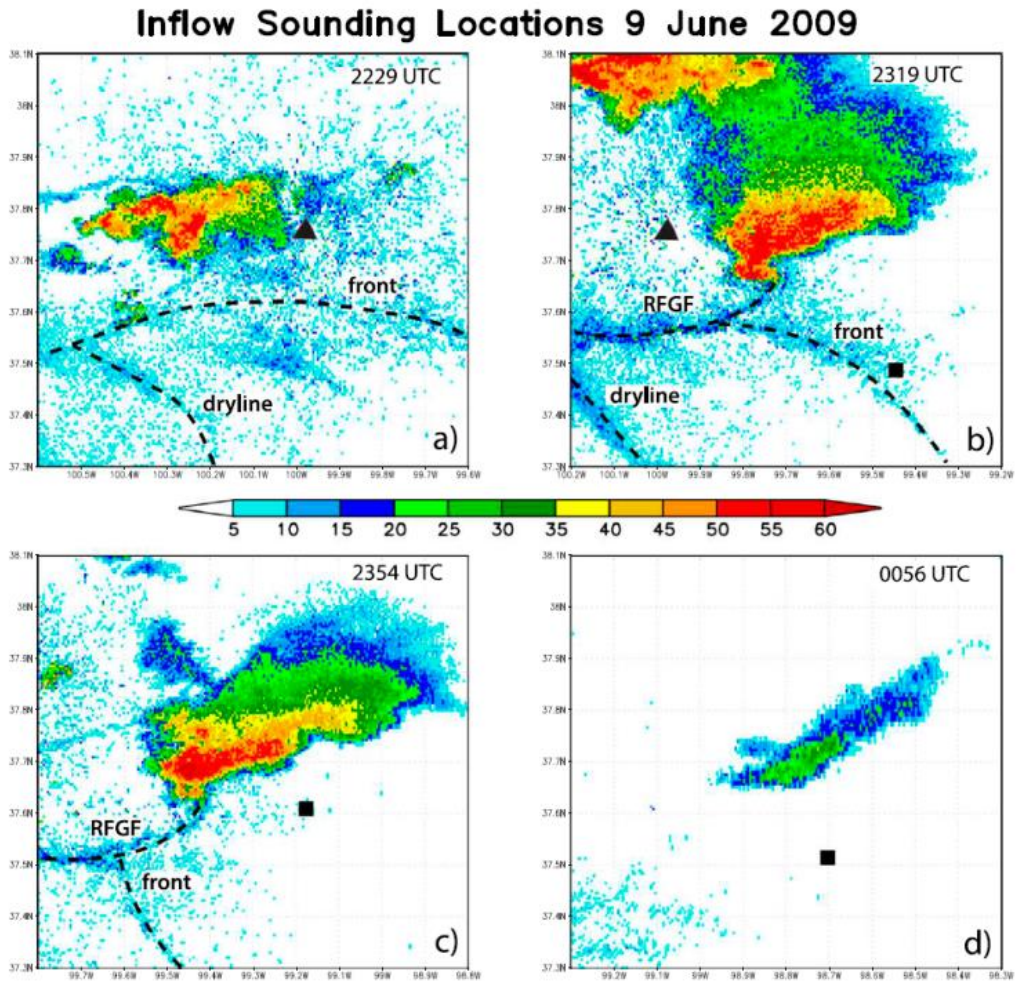

FIGURE 15: Taken from Davenport and Parker (2015a), their figure 2. Base reflectivity from the Dodge City, KS WSR-88D [denoted by the black triangle in (a), (b)] depicting the evolution of the storm over time in relation to the launches of the near-inflow soundings [denoted by the black squares in (b)-(d), starting at 2319 UTC]. Dashed lines represent boundaries that interacted with the cell.

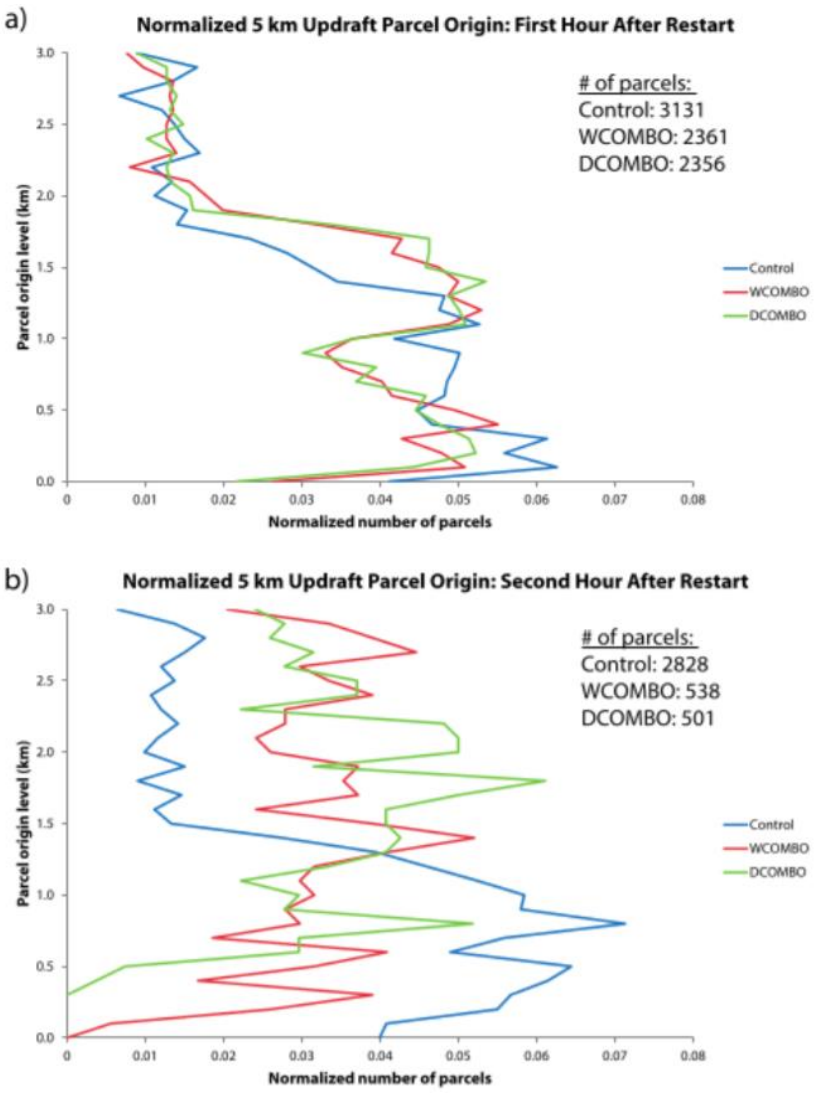

FIGURE 16: Taken from Davenport and Parker (2015b), their figure 6. Histograms of the number of updraft parcels at 5km, binned by parcel origin level during the first and second hour of the simulation.

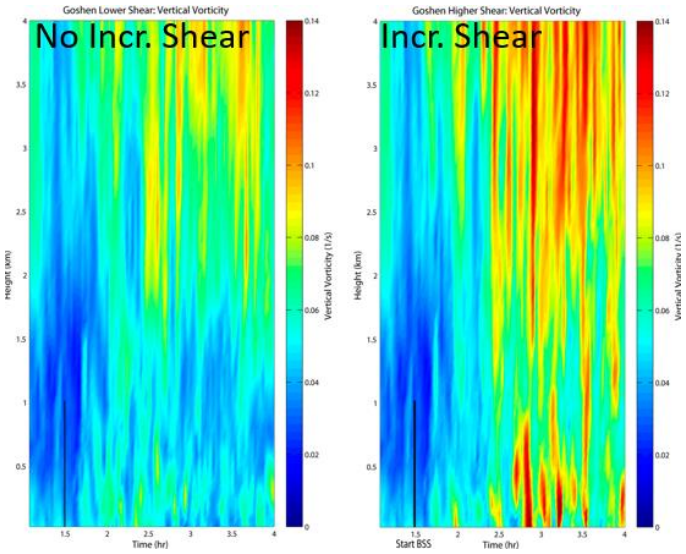

a)

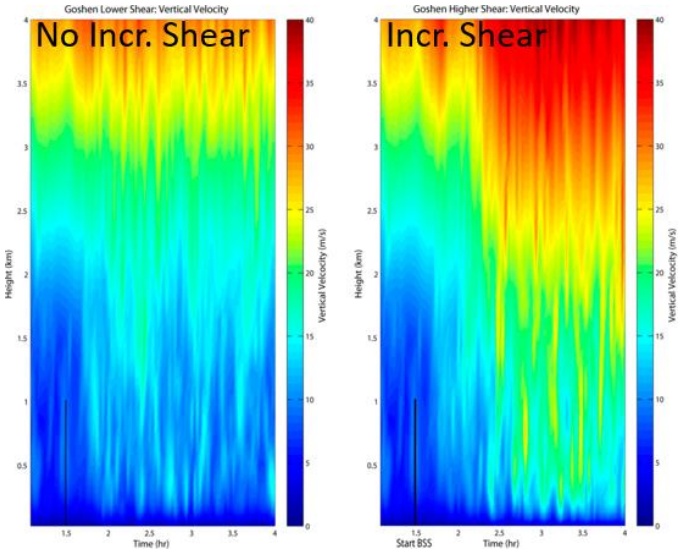

b)

FIGURE 17: Taken from Coffer and Parker (2015), their figures 4 and 5. Time-height plot of the max vertical vorticity (s^{-1}) (a) and max vertical velocity (m s^{-1}) (b) in a 50 km by 50 km box following the supercell's mesocyclone for both (left) the lower shear Goshen Control simulation and (right) the higher-shear Goshen BSS simulation. The BSS began at 1.5h, indicated by the dark line on each picture.

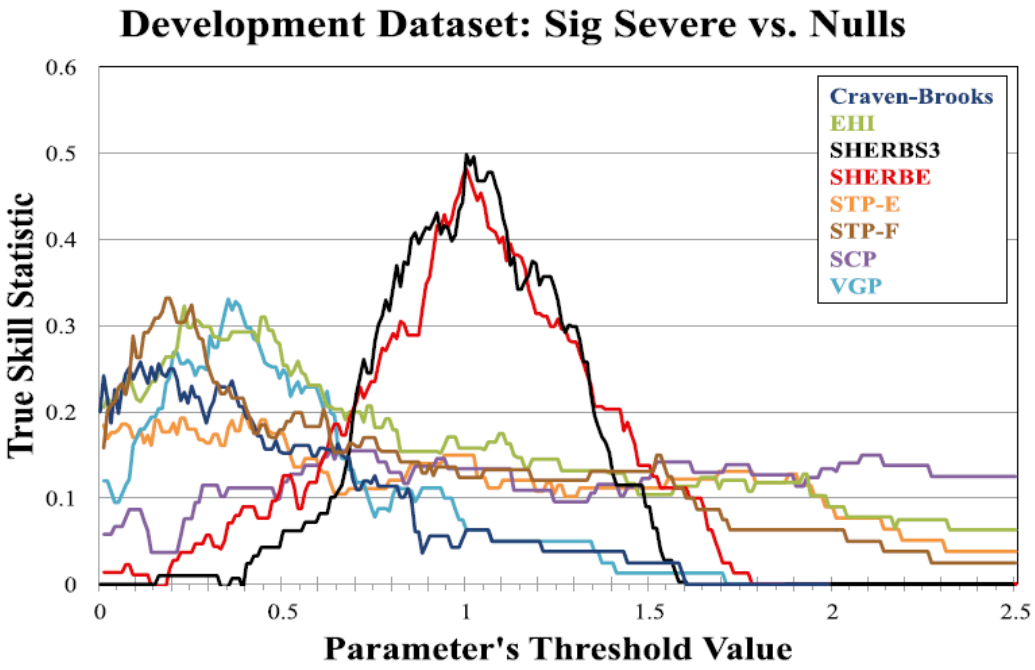

FIGURE 18: Taken from Sherburn and Parker (2014, their figure 6a. True skill score (TSS) for discriminating between HSLC significant severe reports and nulls as a function of parameter threshold value for the given composite parameters in the development dataset. The y axis represents each parameter's TSS [i.e., difference between Probability of Detection (POD) and Probability of False Detection (POFD)] calculated for each possible threshold value along the x axis (i.e., this is a representation of a parameter's potential skill, not its distribution).

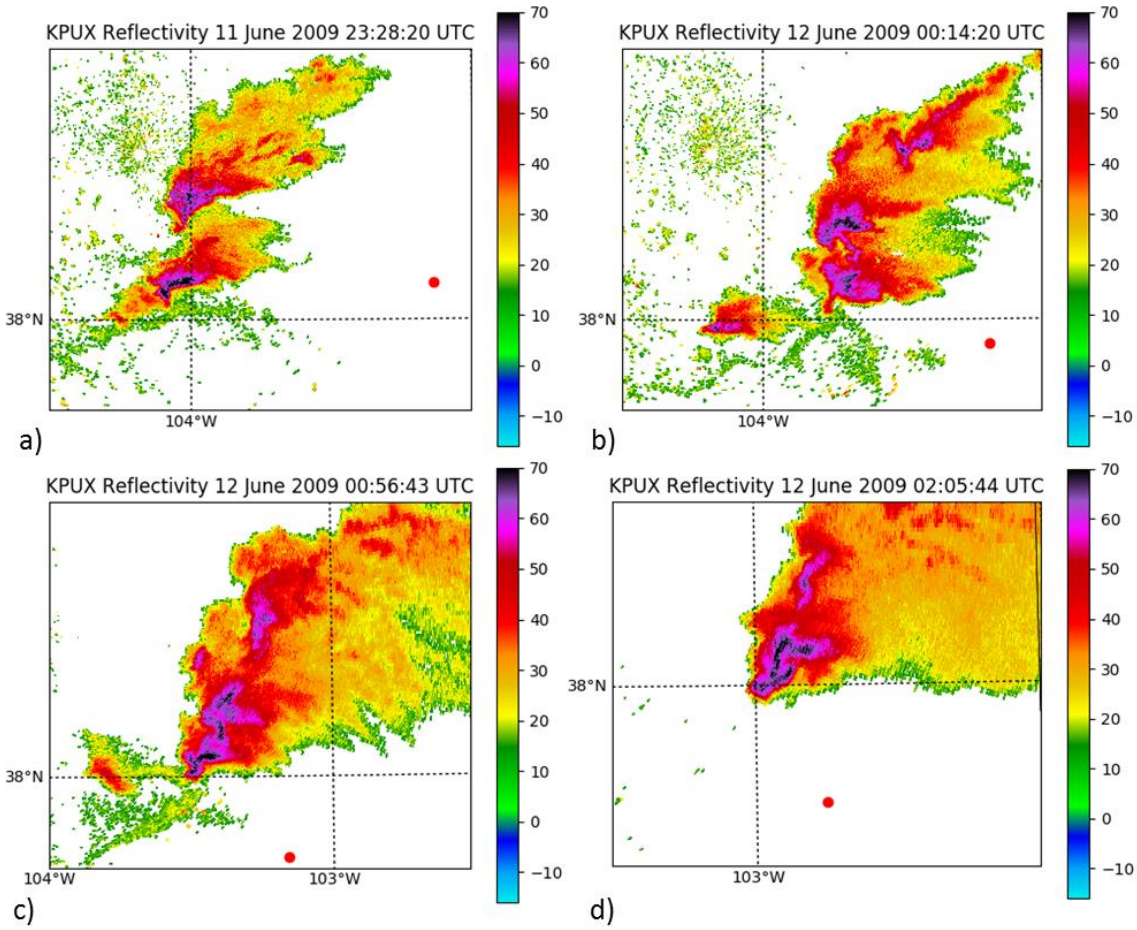

FIGURE 19: Locations of the soundings (indicated by red dots) overlaid on the closest base reflectivity in regards to time from KPUX. Soundings were launched at a) 2329 UTC b) 0014 UTC c) 0058 UTC and d) 0206 UTC.

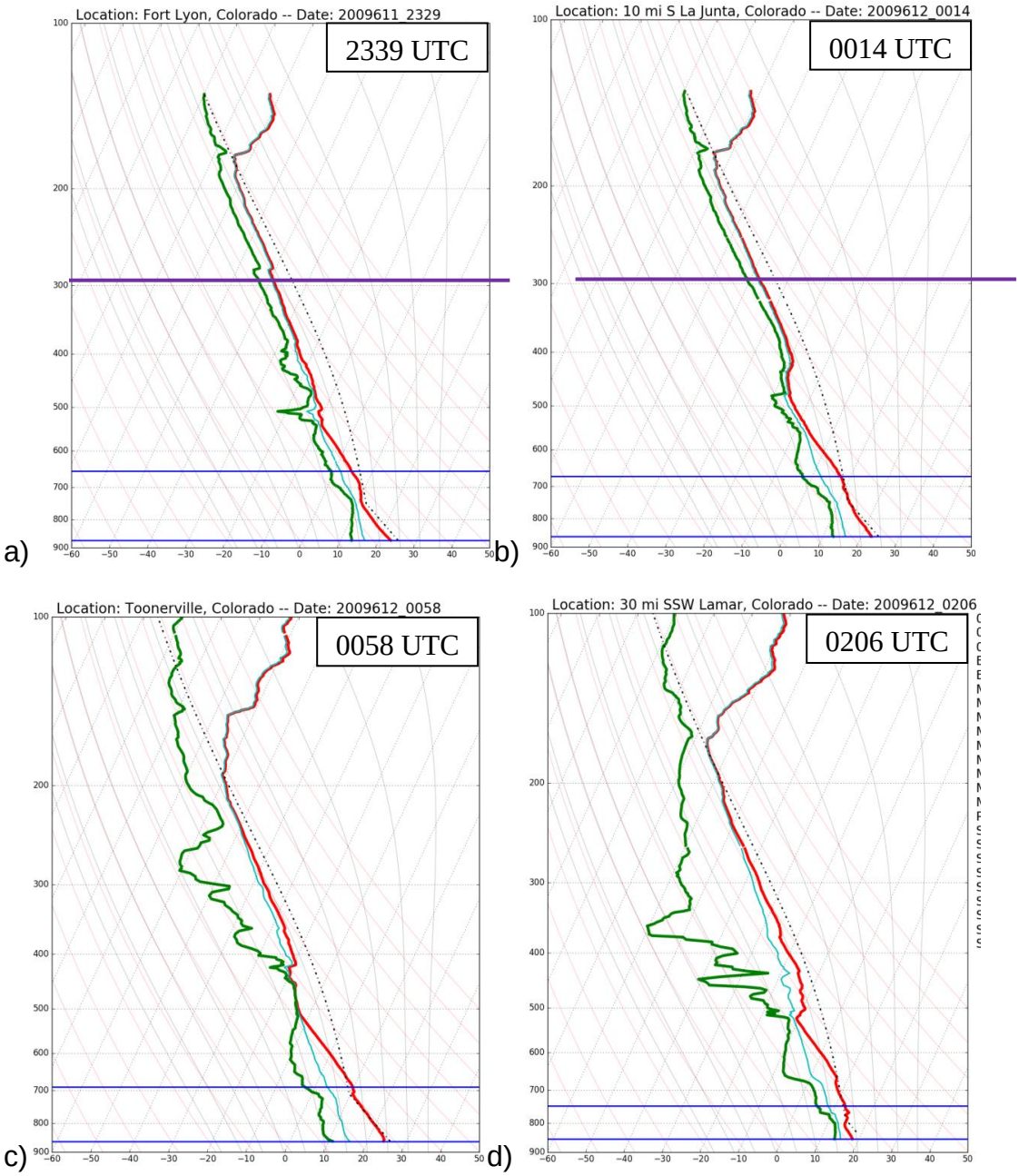

FIGURE 20: VORTEX2 sounding launches at a) 2329 UTC, b) 0014 UTC, c) 0058 UTC, and d) 0206 UTC. The two solid blue lines represent the effective inflow region, which is defined by the Storm Prediction Center (SPC) as the potential thunderstorm inflow layer. The horizontal purple line in a) represents the bottom of the region where data from the 0014 UTC (b) sounding was used to replace missing data.

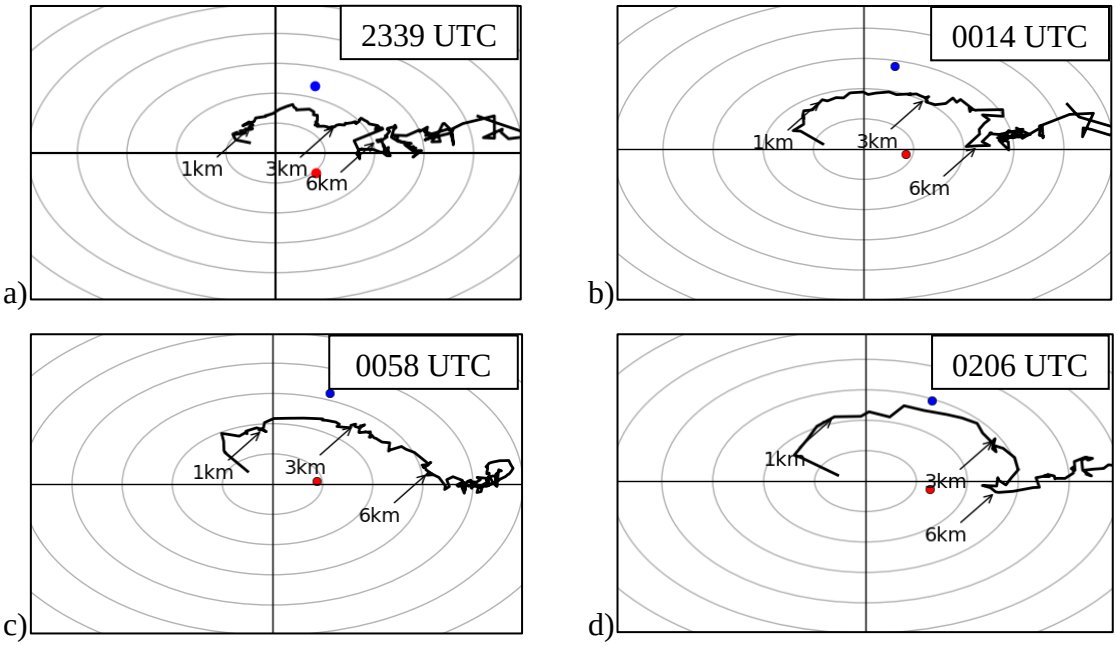

FIGURE 21: Hodographs from the four sounding launches at a) 2329 UTC b) 0014 UTC c) 0058 UTC, d) 0206 UTC. The blue dot represents the Bunkers left moving supercell storm motion vector, and the red dot represents the Bunkers right moving supercell storm motion vector.

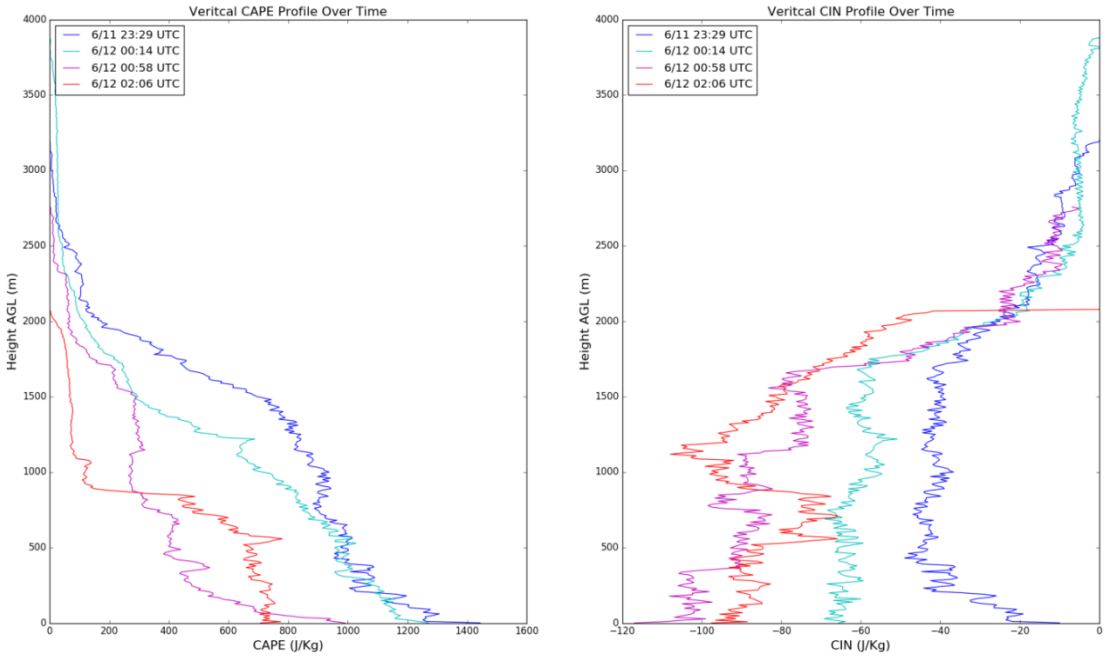

FIGURE 22: Vertical profiles of CAPE (left) and CIN (right) over time for each of the four inflow soundings.

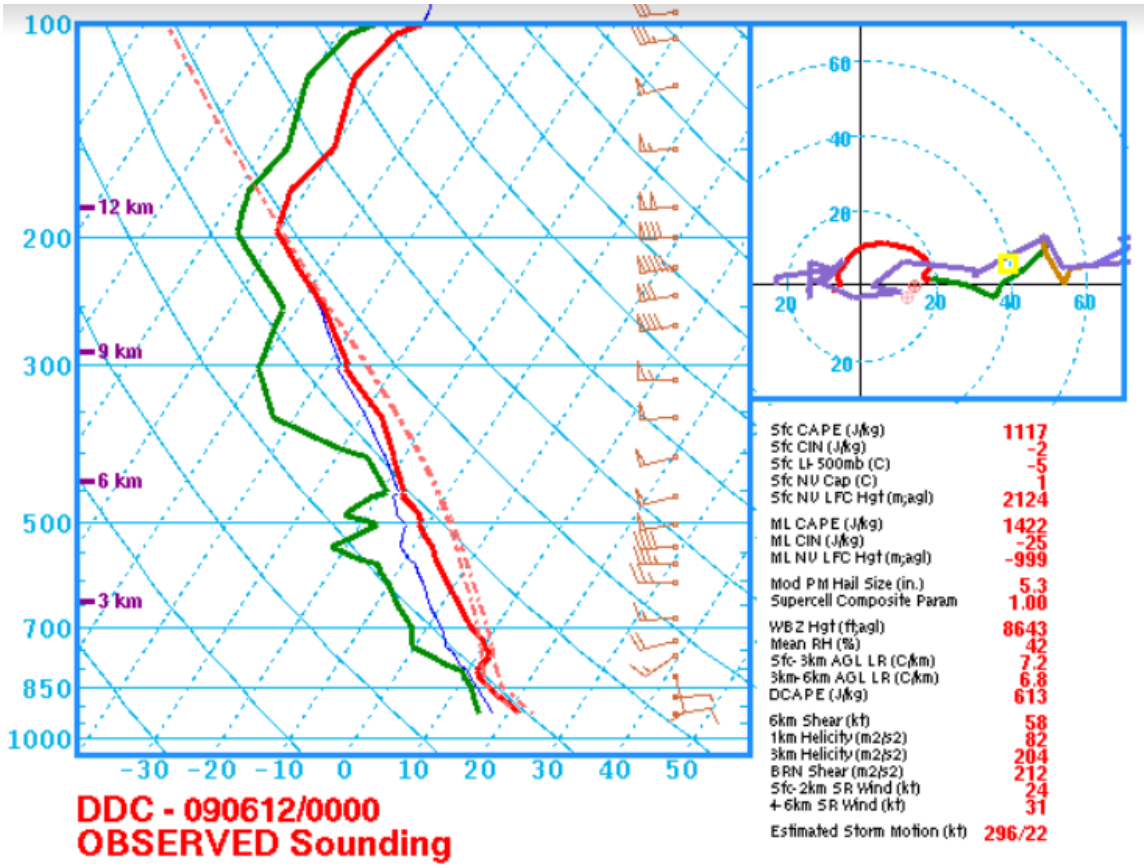

FIGURE 23: Sounding launh from the Dodge City, KS NWS office on 12 June 2009 at 00:00 UTC.

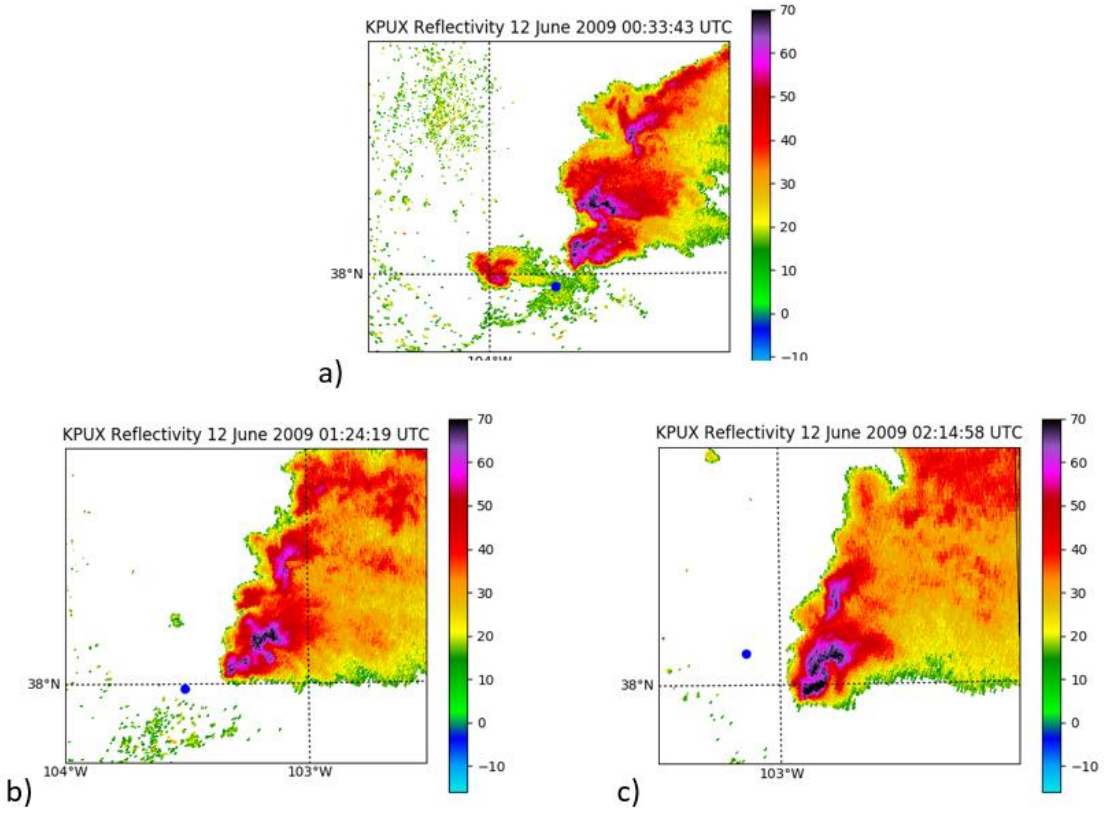

FIGURE 24: As in figure 14, but for locations of RFD soundings.

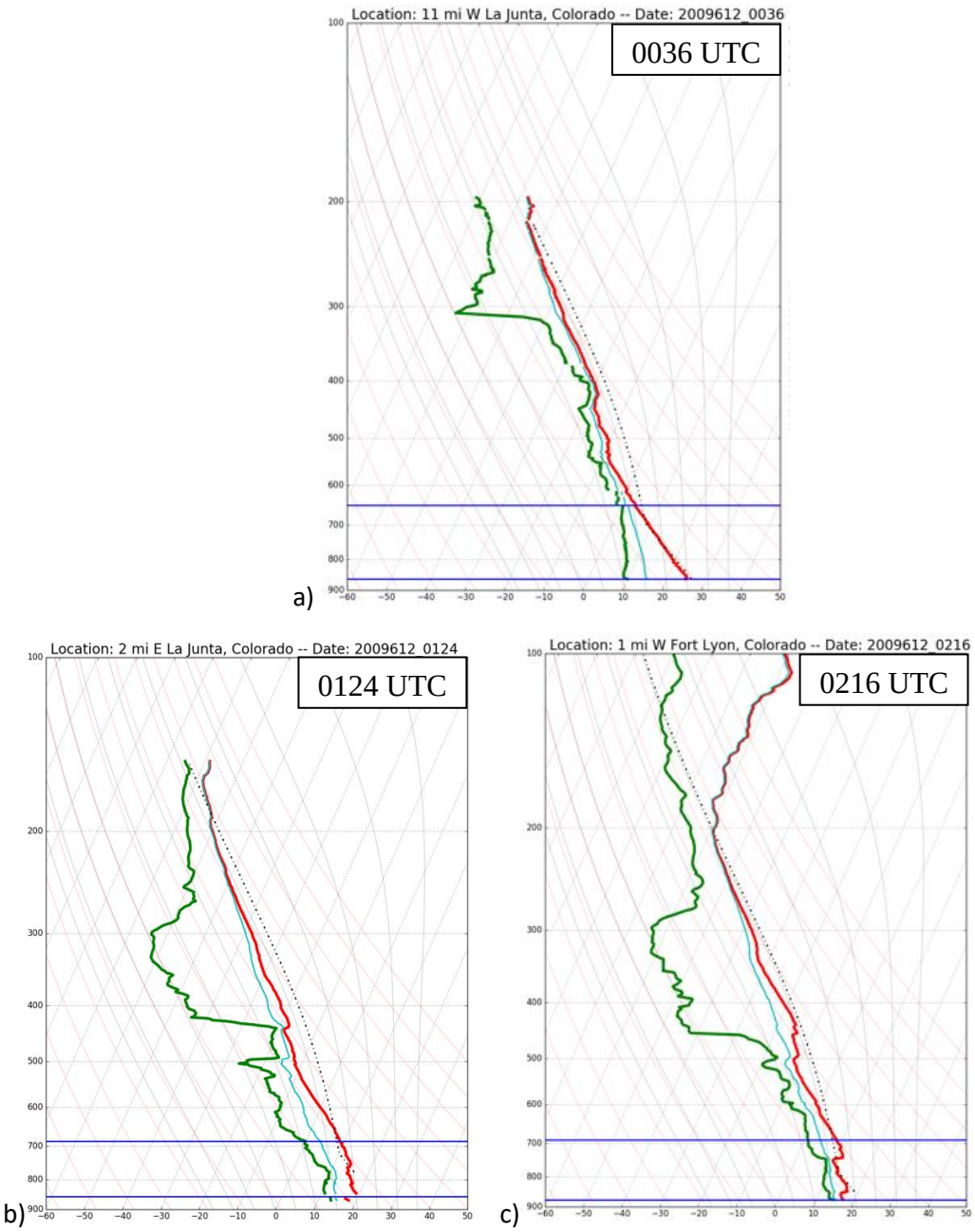

FIGURE 25: As in Fig. 20, but for soundings launched in the RFD region. a) 0036 UTC, b) 0124 UTC, c) 0216 UTC.

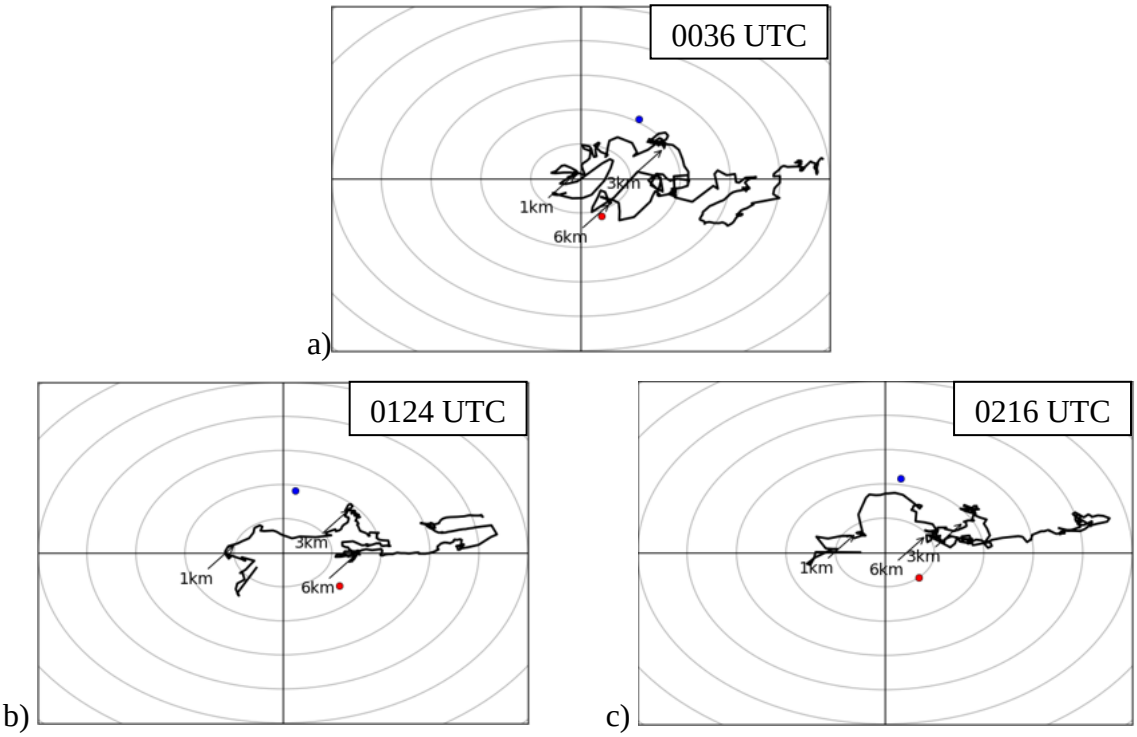

FIGURE 26: As in Fig. 18, but for soundings launched in the RFD region. a) 0036 UTC, b) 0124 UTC, c) 0216 UTC.

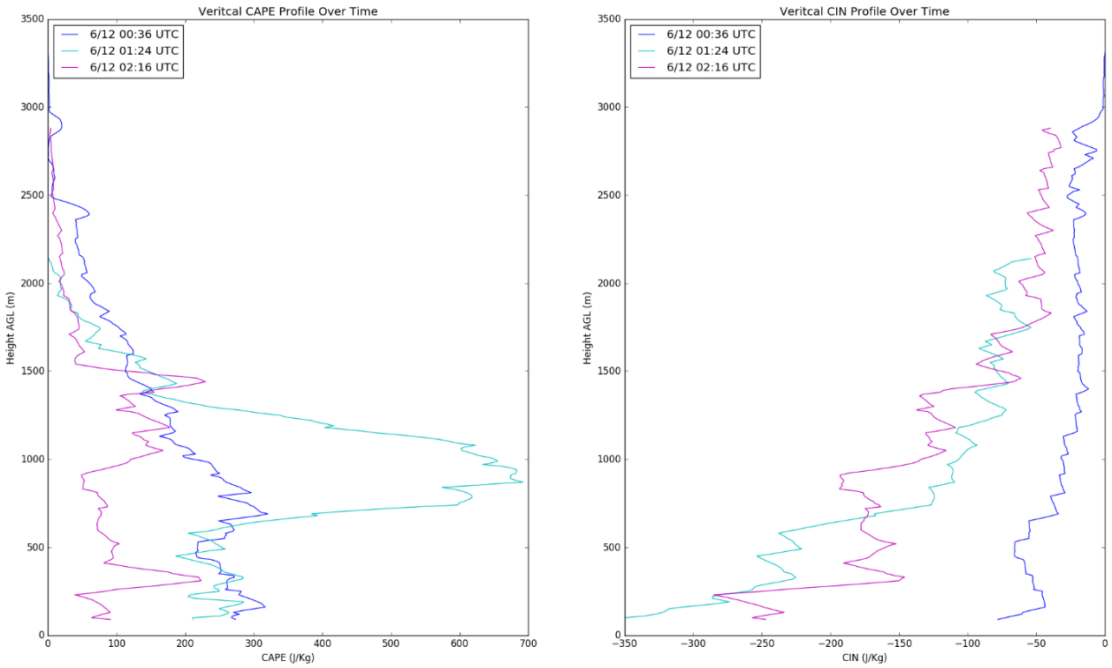

FIGURE 27: As in Fig. 21, but for the 3 RFD Soundings

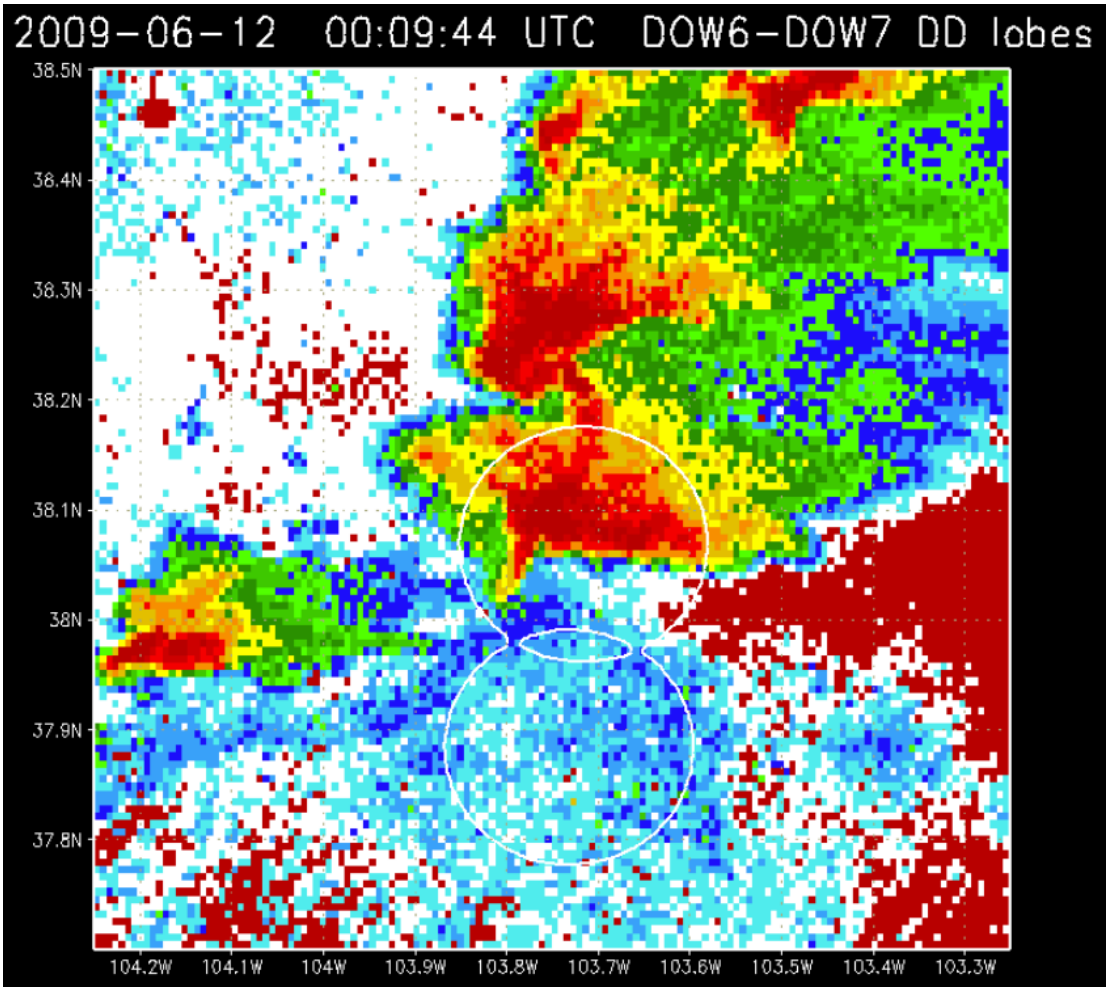

FIGURE 28: Example of dual doppler lobes (white circles) for the DOW6 and DOW7 radars at 00:09:44 UTC.

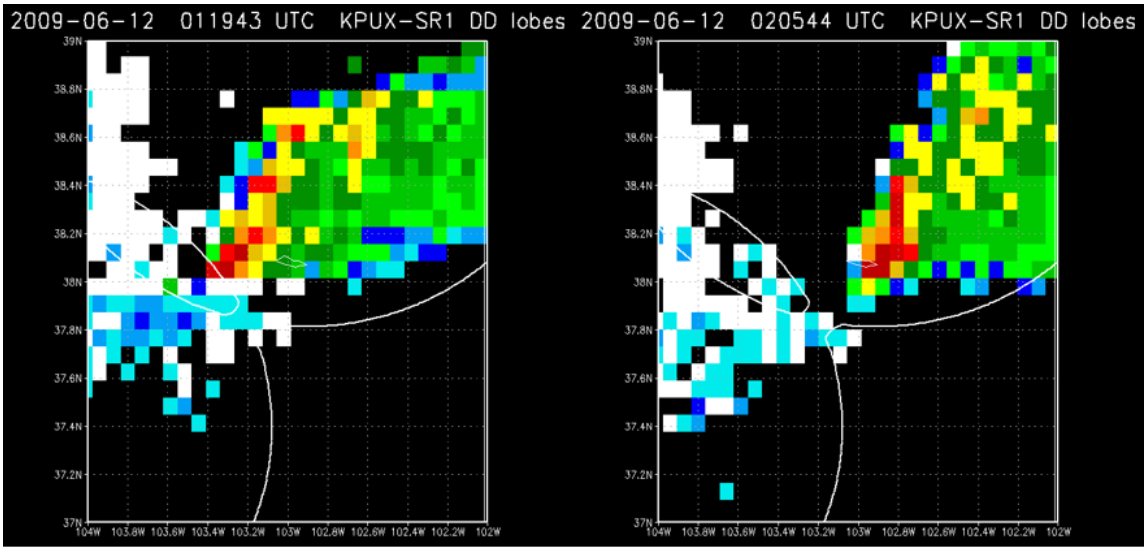

FIGURE 29: Dual-Doppler lobes for KPUX and SR1 at the first and last available time periods for DDA.

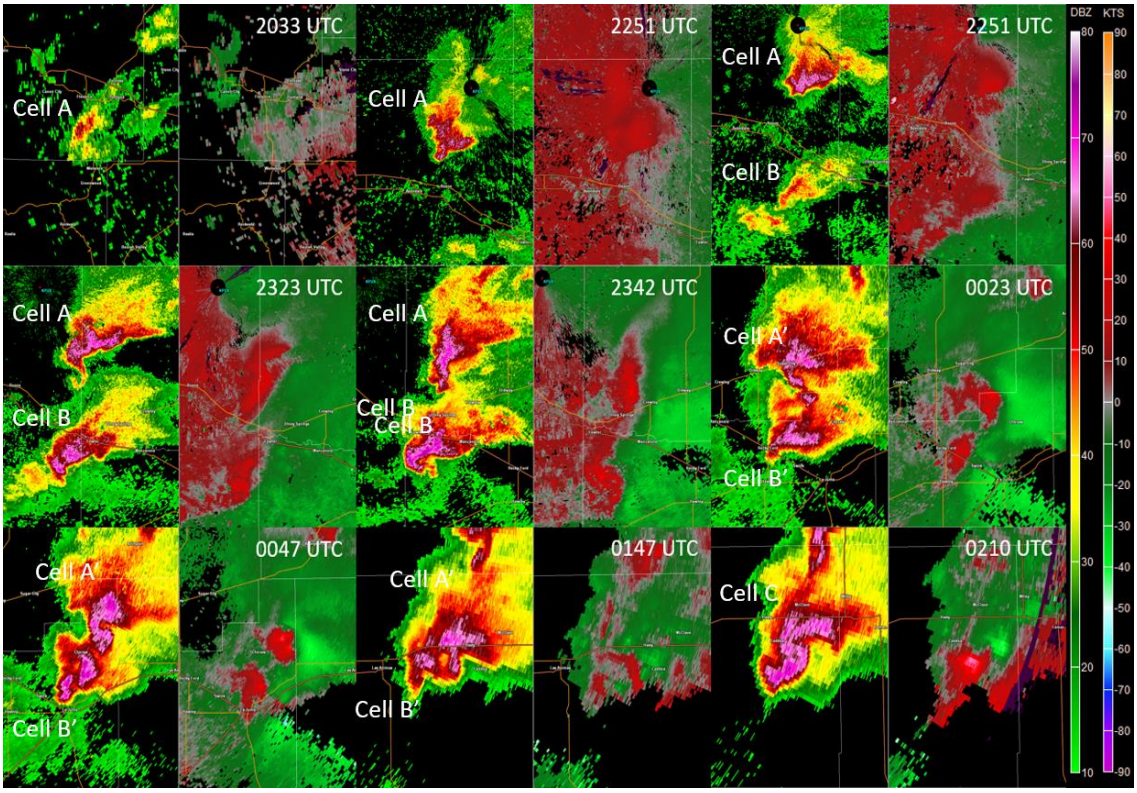

FIGURE 30: Radar overview of the 11-12 June 2009 supercell pair, using KPUX radar reflectivity and Doppler velocities.

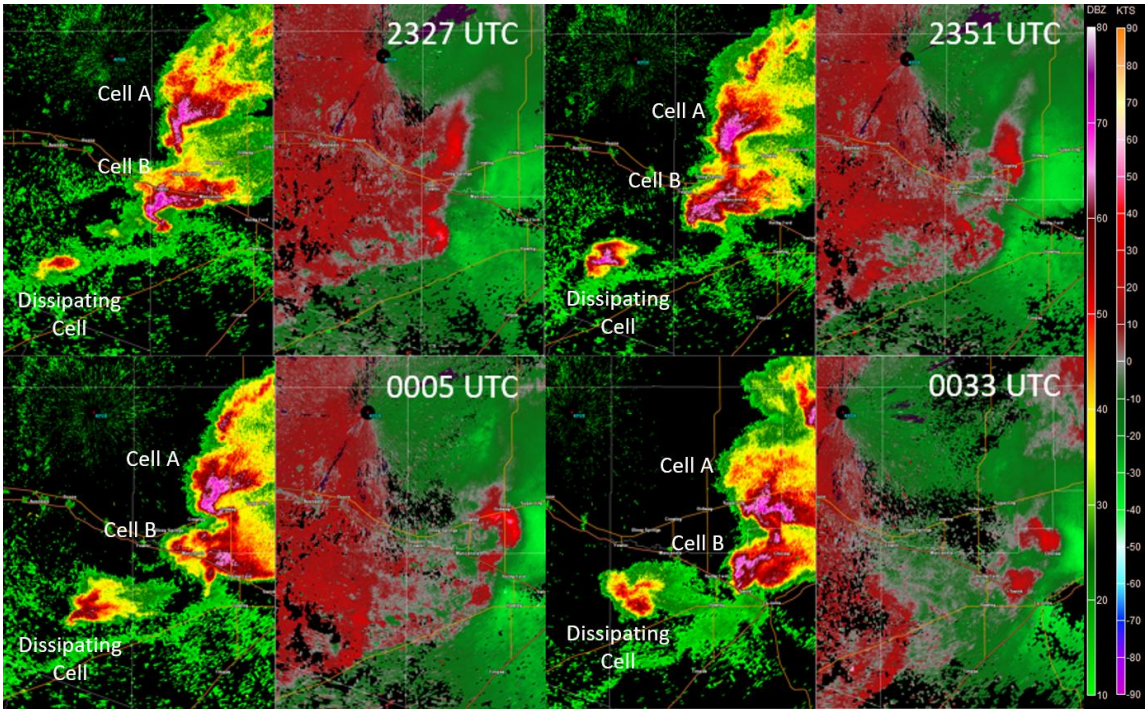

FIGURE 31: Evolution of a short lived supercell that tried to form along the gust fron of Cell B, but dissapated within a couple of hours.

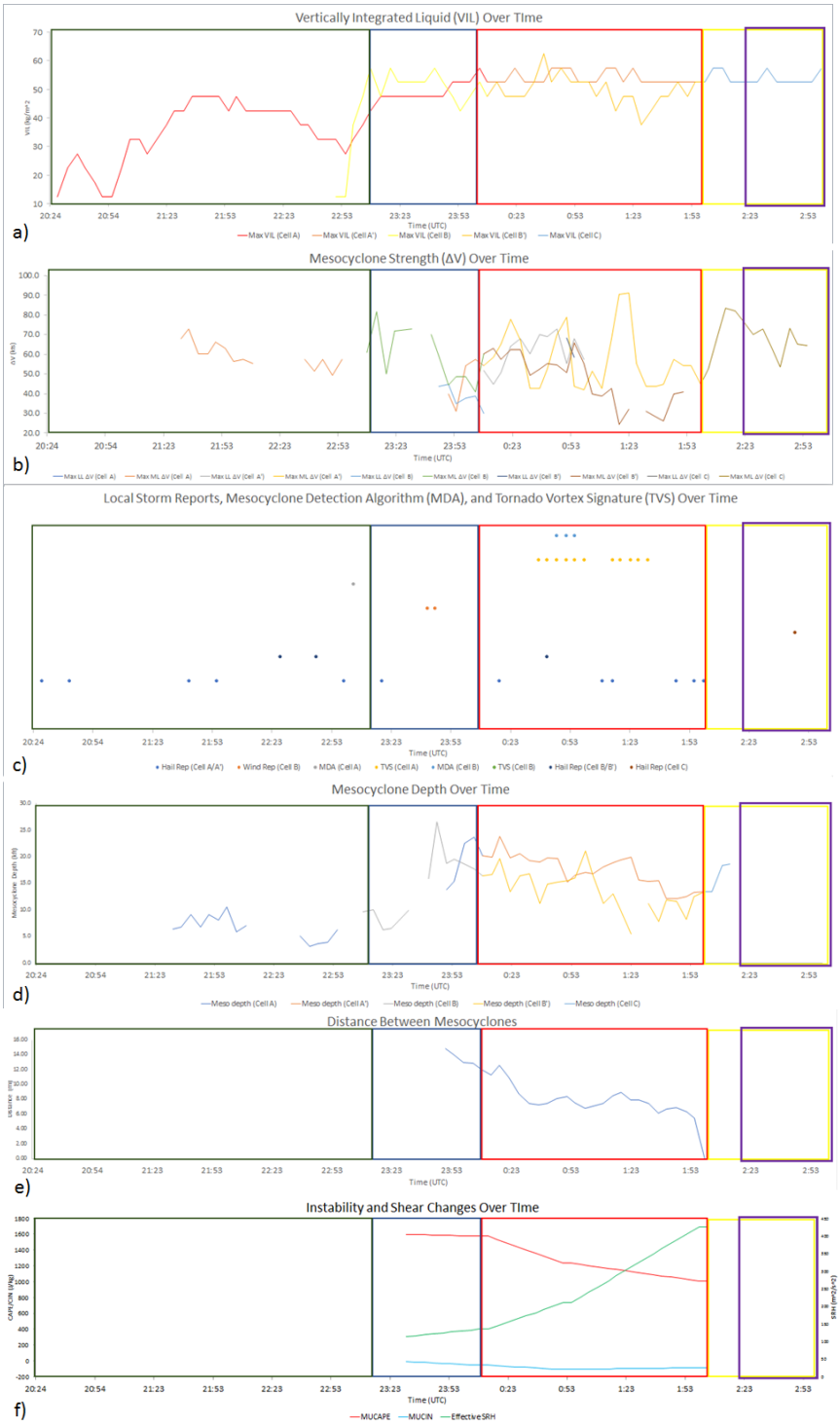

FIGURE 32: Plots of several variables over the period of examinaton for the supercell pair. a) VIL b) mesocyclone intensities at various levels, c) local storm reports and TVS/MDA, d) mesocyclone depth, e) distance between mesocyclones, f) changes in CAPE, CIN and SRH with time. Where the green, blue, red, and yellow outlined portions of the graph represent the baseline, pre-merger, merger, and post-merger phases respectively, and the purple box indicates the nocturnal transition, marked by the period starting one hour prior to sunset, as defined in Gropp and Davenport (2018).

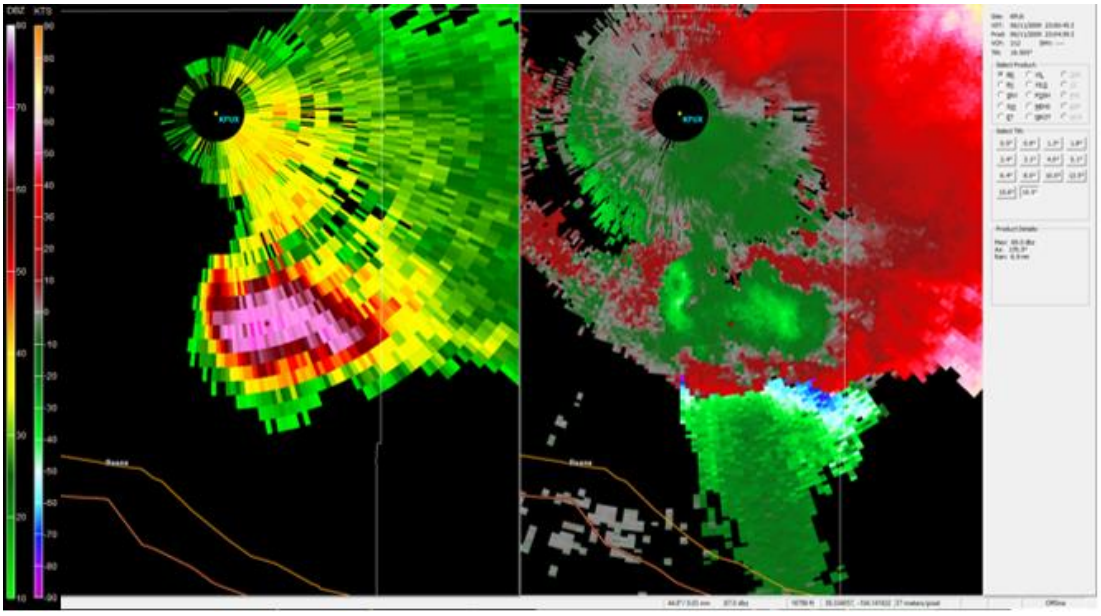

FIGURE 33: Radar screen capture from 23:00 UTC of Cell A, illustrating how close the cell passes to the KPUX Doppler radar. With a max beam height of only around 17kft in the storm, it is likely that the entire mesocyclone is not being seen.

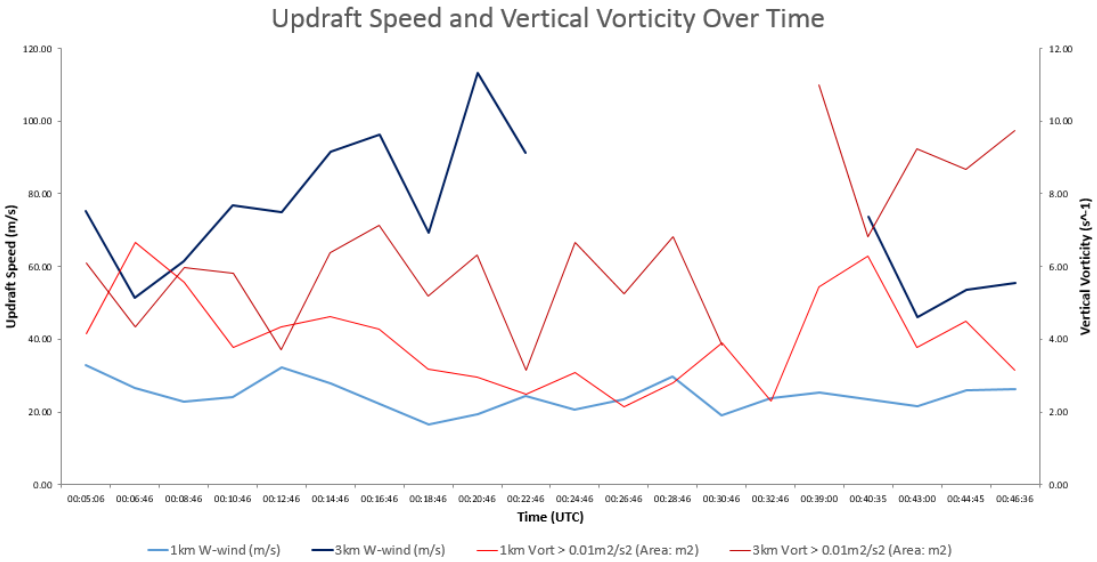

FIGURE 34: Time seies of updraft speed and vertial vorticity at 1km and 3km AGL as computed during dual-Doppler analysis.

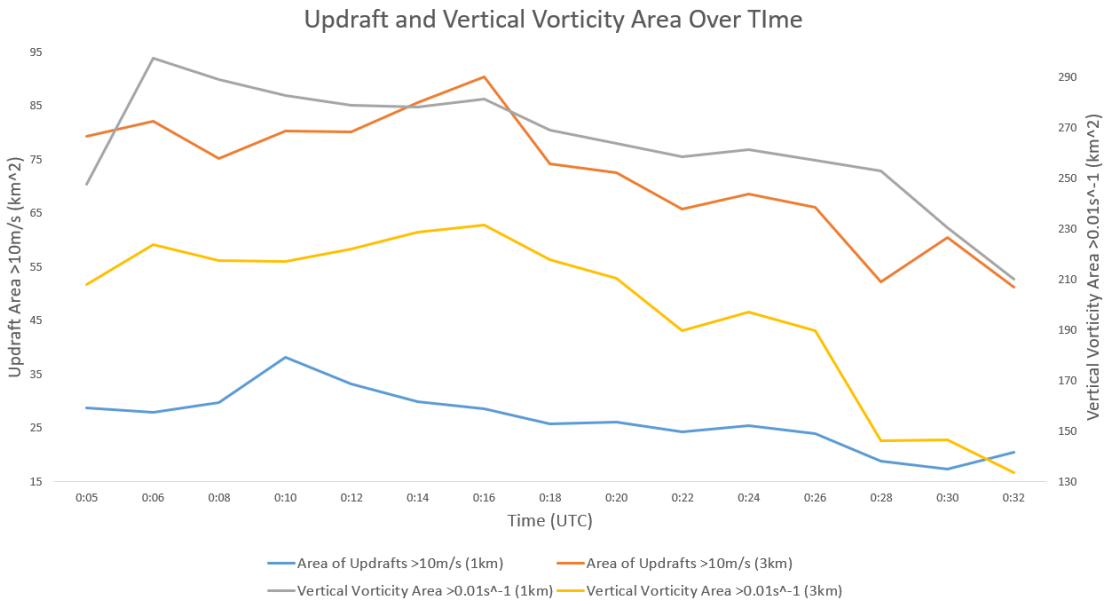

FIGURE 35: As in figure 34, but for updraft area >10m/s and the vertical vorticity area >10s^{-1}

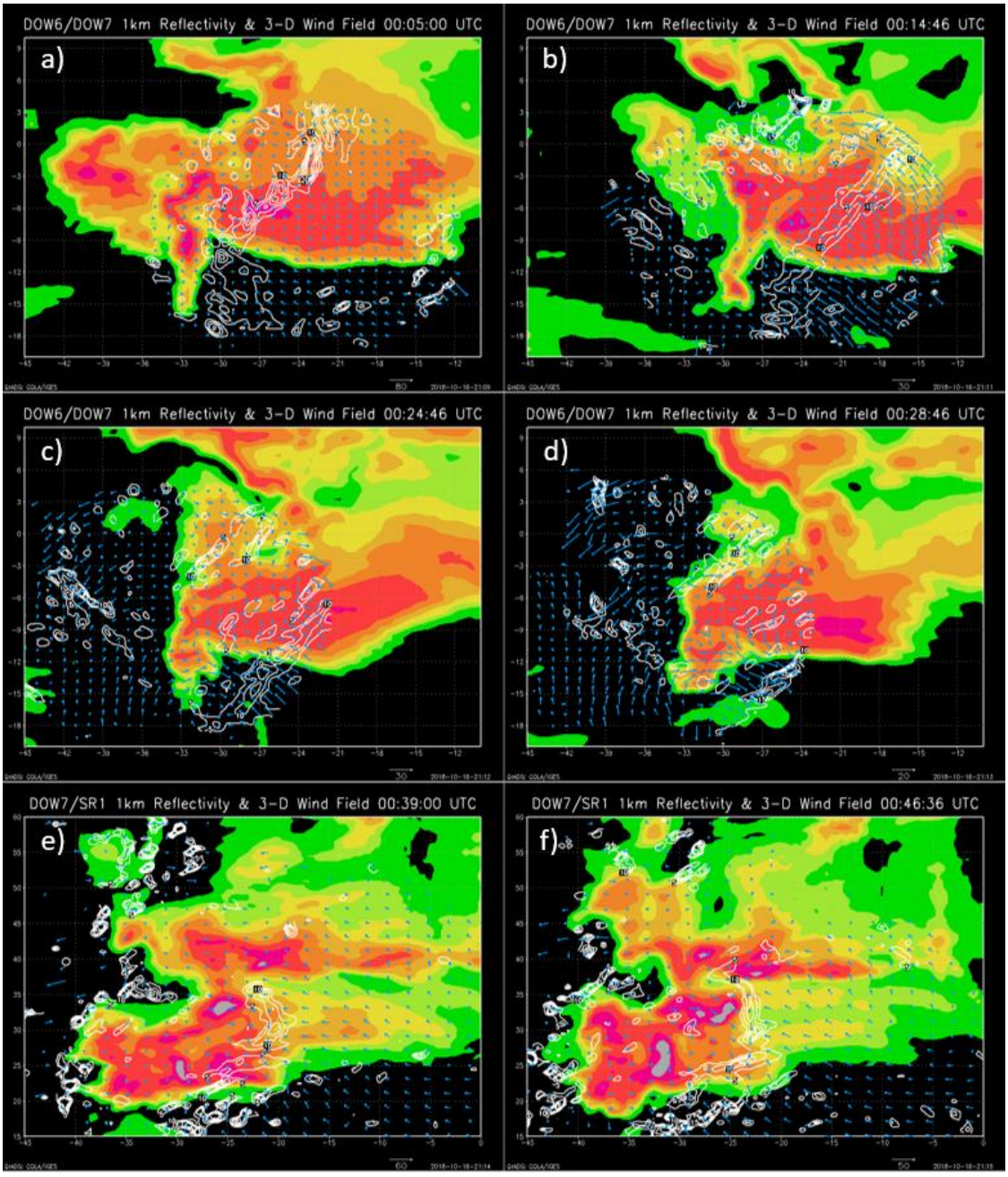

FIGURE 36: Plot of reflectivity (colors), horizontal wind vectors (cyan arrows), and updraft speed in meters/second (white contours). The axes represent distance in km from the zero point in each direction, which is just how large the grid was that is used to plot the image. Times were randomly picked just to illustrate the overall evolution of the cells.

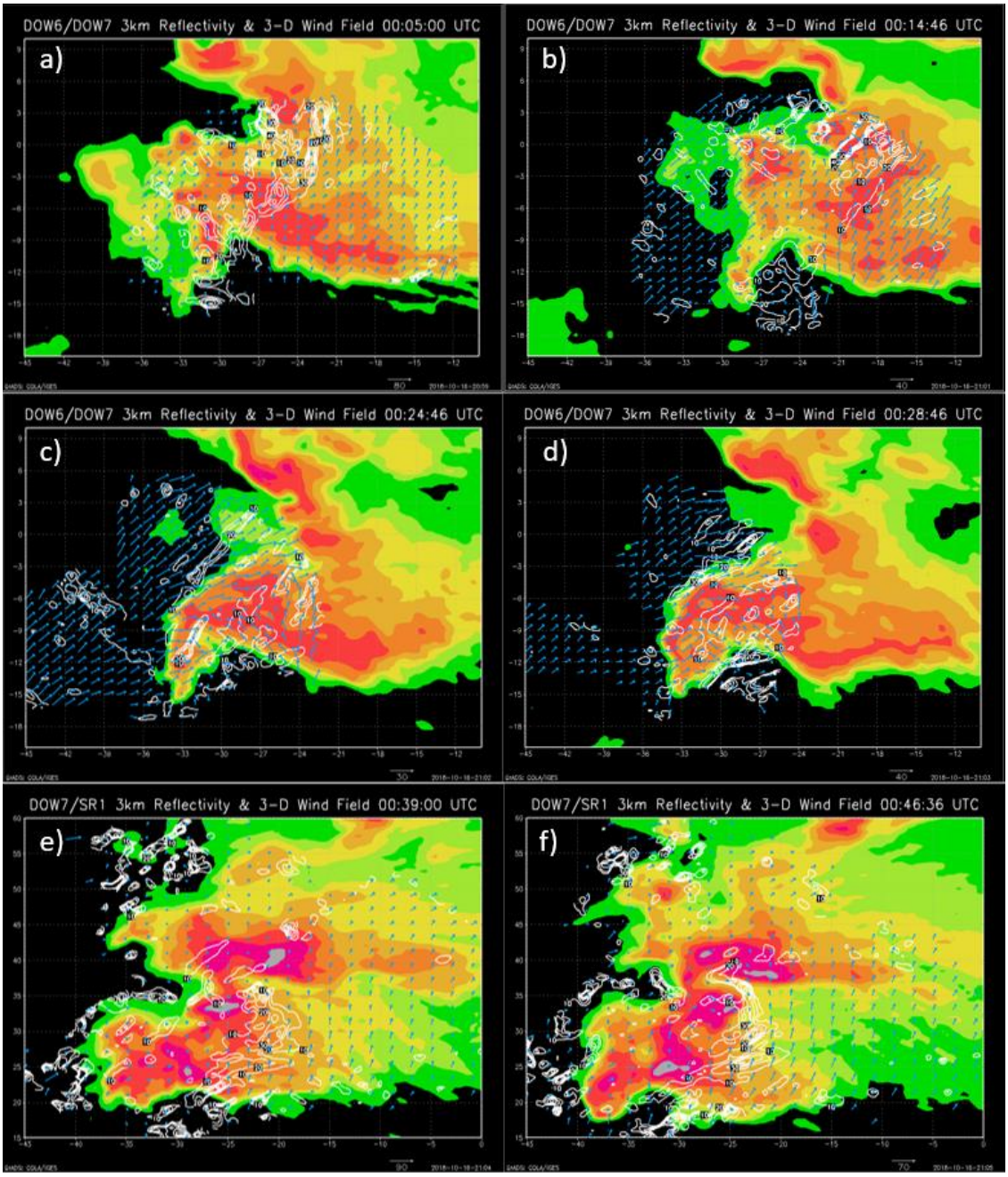

FIGURE 37: As in Fig. 21, but the white countour represents the updraft strength at 3km instead.

REFERENCES

Barker III, L. 2006: 3.6 A Potentially Valuable WSR-88D Severe Storm Pre-Cursor Signature in Highly Dynamic, Low CAPE, High Shear Environments (2006 - 23SLS_23sls). *23rd Conference on Local Severe Storms*. n.p., https://ams.confex.com/ams/23SLS/techprogram/paper_115129.htm

Barnes, S. L., 1964: A technique for maximizing details in numerical weather map analysis. J. Appl. Meteor., 3, 396–409, doi:10.1175/1520-0450(1964)003,0396:ATFMDI.2.0.CO;2.

Biggerstaff, M., et al. 2012. Mobile SMART-R1 Radar Data. Version 1.0. UCAR/NCAR - Earth Observing Laboratory. https://data.eol.ucar.edu/dataset/114.144.

Biggerstaff, M.I., L.J. Wicker, J. Guynes, C. Ziegler, J.M. Straka, E.N. Rasmussen, A. Doggett, L.D. Carey, J.L. Schroeder, and C. Weiss, 2005: The Shared Mobile Atmospheric Research and Teaching Radar: A Collaboration to Enhance Research and Teaching. Bull. Amer. Meteor. Soc., 86, 1263–1274, https://doi.org/10.1175/BAMS-86-9-1263

Bluestein, H.B. and M.L. Weisman, 2000: The Interaction of Numerically Simulated Supercells Initiated along Lines. Mon. Wea. Rev., 128, 3128–3149, https://doi.org/10.1175/1520-0493(2000)128<3128:TIONSS>2.0.CO;2

Blumberg, W.G., K.T. Halbert, T.A. Supinie, P.T. Marsh, R.L. Thompson, and J.A. Hart, 2017: SHARPpy: An Open-Source Sounding Analysis Toolkit for the Atmospheric Sciences. Bull. Amer. Meteor. Soc., 98, 1625–1636, https://doi.org/10.1175/BAMS-D-15-00309.1

Clark, M. R., 2009: The Southern England Tornadoes of 30 December 2006: Case Study of a Tornadic Storm in a Low CAPE, High Shear Environment. *Atmospheric Research* 93 (s 1–3) (July 1): 50–65. doi:10.1016/j.atmosres.2008.10.008.

Coffer, B.E. and M.D. Parker, 2015: Impacts of Increasing Low-Level Shear on Supercells during the Early Evening Transition. Mon. Wea. Rev., 143, 1945–1969, https://doi.org/10.1175/MWR-D-14-00328.1

Davenport, C.E. and M.D. Parker, 2015: Observations of the 9 June 2009 Dissipating Supercell from VORTEX2. Wea. Forecasting, 30, 368–388, https://doi.org/10.1175/WAF-D-14-00087.1

Davenport, C.E. and M.D. Parker, 2015: Impact of Environmental Heterogeneity on the Dynamics of a Dissipating Supercell Thunderstorm. Mon. Wea. Rev., 143, 4244 4277,https://doi.org/10.1175/MWR-D-15-0072.1

French, A.J. and M.D. Parker, 2012: Observations of Mergers between Squall Lines and Isolated Supercell Thunderstorms. Wea. Forecasting, 27, 255–278, https://doi.org/10.1175/WAF-D-11-00058.1

Guyer, J., and A. Dean, 2010: Tornadoes Within Weak CAPE Environments Across the Continental United States (2010 - 25SLS_25sls). *25th Conference on Local Severe Storms*. n.p., https://ams.confex.com/ams/25SLS/techprogram/paper_175725.htm

Gropp, M.E. and C.E. Davenport, 2018: The Impact of the Nocturnal Transition on the Lifetime and Evolution of Supercell Thunderstorms in the Great Plains. Wea. Forecasting, 33, 1045–1061, https://doi.org/10.1175/WAF-D-17-0150.1

Hastings, R. and Y. Richardson, 2016: Long-Term Morphological Changes in Simulated Supercells Following Mergers with Nascent Supercells in Directionally Varying Shear. Mon. Wea. Rev., 144, 471–499, https://doi.org/10.1175/MWR-D150193.1

Lemon, L.R. and C.A. Doswell, 1979: Severe Thunderstorm Evolution and Mesocyclone Structure as Related to Tornadogenesis. Mon. Wea. Rev., 107, 1184–1197, https://doi.org/10.1175/1520-0493(1979)107<1184:STEAMS>2.0.CO;2

Majcen, M., P. Markowski, Y. Richardson, D. Dowell, and J. Wurman, 2008: Multipass Objective Analyses of Doppler Radar Data. J. Atmos. Oceanic Technol., 25, 18451858, https://doi.org/10.1175/2008JTECHA1089.1

Markowski, P.M. and J.M. Straka, 2000: Some Observations of Rotating Updrafts in a Low Buoyancy, Highly Sheared Environment. Mon. Wea. Rev., 128, 449–461, https://doi.org/10.1175/1520-0493(2000)128<0449:SOORUI>2.0.CO;2

McCaul, E.W. and M.L. Weisman, 2001: The Sensitivity of Simulated Supercell Structure and Intensity to Variations in the Shapes of Environmental Buoyancy and Shear Profiles. Mon. Wea. Rev., 129, 664–687, https://doi.org/10.1175/1520-0493(2001)129<0664:TSOSSS>2.0.CO;2

NEXRAD Technical Information, www.roc.noaa.gov/WSR88D/Engineering/NEXRADTechInfo.aspx.

Nowotarski, C.J., P.M. Markowski, and Y.P. Richardson, 2011: The Characteristics of Numerically Simulated Supercell Storms Situated Over Statically Stable Boundary Layers. Mon. Wea. Rev., 139:10, 3139-3162

Pauley, P.M. and X. Wu, 1990: The Theoretical, Discrete, and Actual Response of the Barnes Objective Analysis Scheme for One- and Two-Dimensional Fields. Mon. Wea. Rev., 118, 1145–1164, https://doi.org/10.1175/1520-0493(1990)118<1145:TTDAAR>2.0.CO;2

Rasmussen, E.N. and D.O. Blanchard, 1998: A Baseline Climatology of Sounding-Derived Supercell andTornado Forecast Parameters. Wea. Forecasting, 13, 1148–1164, https://doi.org/10.1175/1520-0434(1998)013<1148:ABCOSD>2.0.CO;2

Rogers, J., J. L. Schroeder, C. Leary, and C. Weiss, 2007: *The Association of Thunderstorm Cell Mergers with Tornado Occurrence*. https://ttu-ir.tdl.org/ttu-ir/handle/2346/15608

Rotunno, R. and J. Klemp, 1985: On the Rotation and Propagation of Simulated Supercell Thunderstorms. J. Atmos. Sci., 42, 271–292, https://doi.org/10.1175/1520-0469(1985)042<0271:OTRAPO>2.0.CO;2

Sherburn, K.D. and M.D. Parker, 2014: Climatology and Ingredients of Significant Severe Convection in High-Shear, Low-CAPE Environments. Wea. Forecasting, 29, 854–877, https://doi.org/10.1175/WAF-D-13-00041.1

Tanamachi, R.L., P.L. Heinselman, and L.J. Wicker, 2015: Impacts of a Storm Merger on the 24 May 2011 El Reno, Oklahoma, Tornadic Supercell. Wea. Forecasting, 30, 501–524, https://doi.org/10.1175/WAF-D-14-00164.1

Thompson, R.L., R. Edwards, J.A. Hart, K.L. Elmore, and P. Markowski, 2003: Close Proximity Soundings within Supercell Environments Obtained from the Rapid Update Cycle. Wea. Forecasting, 18, 1243–1261, https://doi.org/10.1175/1520-0434(2003)018<1243:CPSWSE>2.0.CO;2

Trapp, R.J. and C.A. Doswell, 2000: Radar Data Objective Analysis. J. Atmos. Oceanic Technol., 17, 105–120, https://doi.org/10.1175/1520-0426(2000)017<0105:RDOA>2.0.CO;2

UCAR/NCAR - Earth Observing Laboratory. 2010. NCAR MGAUS Radiosonde Data. Version 1.0. UCAR/NCAR - Earth Observing Laboratory. https://doi.org/10.5065/D6MW2FGW

Wurman, J., 2001: The DOW mobile multiple-Doppler network. Preprints, 30th Int. Conf. on Radar Meteorology, Munich, Germany, Amer. Meteor. Soc., P3.3. [Available online at https://ams.confex.com/ams/pdfpapers/21572.pdf.]

Wurman, J., J. Straka, E. Rasmussen, M. Randall, and A. Zahrai, 1997: Design and Deployment of a Portable, Pencil-Beam, Pulsed, 3-cm Doppler Radar. J. Atmos. Oceanic Technol., 14, 1502–1512, https://doi.org/10.1175/15200426(1997)014<1502:DADOAP>2.0.CO;2

Wurman, J., Y. Richardson, C. Alexander, S. Weygandt, and P.F. Zhang, 2007: Dual Doppler and Single-Doppler Analysis of a Tornadic Storm Undergoing Mergers \

and Repeated Tornadogenesis. Mon. Wea. Rev., 135, 736–758, https://doi.org/10.1175/MWR3276.1

Wurman, J., Kosiba, K., Center for Severe Weather Research (CSWR). 2011. Mobile DOW-6 Data. Version 1.0. UCAR/NCAR - Earth Observing Laboratory. https://data.eol.ucar.edu/dataset/114.102.

Wurman, J., Kosiba, K., Center for Severe Weather Research (CSWR). 2011. Mobile DOW-7 Data. Version 1.0. UCAR/NCAR - Earth Observing Laboratory. https://data.eol.ucar.edu/dataset/114.103.